Amorphization and Ablation of Crystalline Silicon Using Ultrafast Lasers: Dependencies on the Pulse Duration and Irradiation Wavelength

Mario Garcia-lechuga, Noemi Casquero, Jan Siegel, Javier Solis, Raphael Clady, Andong Wang, Olivier Utéza, David Grojo

LASER & PHOTONICS REVIEWS
www.lpr-journal.org

Amorphization and Ablation of Crystalline Silicon Using Ultrafast Lasers: Dependencies on the Pulse Duration and Irradiation Wavelength

Mario Garcia-Lechuga, Noemi Casquero, Jan Siegel, Javier Solis, Raphael Clady, Andong Wang, Olivier Utéza, and David Grojo*

Using lasers to achieve controlled crystallographic phase changes in silicon with high spatial precision promises new manufacturing solutions in semiconductor technologies, including silicon photonics. Recent demonstrations of improved amorphization thicknesses position ultrafast lasers as an optimum tool to meet current challenges. Here, the literature on silicon transformations is reviewed and complemented with new experimental data. This includes amorphization and ablation response as a function of pulse duration ($\tau = 13.9$ to 134 fs at $\lambda = 800$ nm) and laser wavelength ($\lambda = 258$ to 4000 nm with $\tau = 200$ fs pulses). For pulse duration-dependent studies on Si(111), the amorphization fluence threshold decreases with shorter durations, emphasizing the significance of non-linear absorption in the range of considered conditions. For wavelength-dependent studies, the amorphization threshold increases sharply from $\lambda = 258$ to 1030 nm, followed by near-constant behavior up to $\lambda = 3000$ nm. Conversely, the ablation threshold fluence increases in these specified ranges. Differences in the obtained amorphization thicknesses on Si(111) and Si(100) are also discussed, identifying an anomalously large fluence range for amorphization at $\lambda = 258$ nm. Finally, the question of the lateral resolution, shown as independent of the interaction nonlinearity is addressed.

1. Introduction

Silicon, an abundant element, serves as the fundamental building block in semiconductor technologies,[1] playing a crucial role in microelectronics, and photovoltaics, and gaining increased interest in the field of photonics. Its applicability to these diverse fields relies on developing strategies that enable the control of its properties. To adjust the electrical ones, the standard approach is doping (n-type or p-type), the basis for the manufacturing of microelectronic components. Doping can additionally be employed to tune optical properties, as exemplified by laser hyperdoping[2] enabling the enhancement of absorption at wavelengths for which pure silicon is transparent. Furthermore, engineering silicon at the nanoscale opens up new possibilities for local tunability of the apparent refractive index.[3] Sub-wavelength structuring enables the fabrication of photonic crystals[4] or light-guiding elements[5] for applications in the infrared domain of the spectrum (transparency range of silicon).

The modifications of silicon for photonic applications are typically carried out using lithographic techniques. The corresponding so-called field of "silicon photonics" often relies on the specific silicon-on-insulator (SOI) technology, an aspect that can cause integration limitations for photonic and electronic elements together on the same platform. In this context, direct laser writing applied to achieve precise transformations of crystalline silicon has become an attractive alternative.

For this perspective, two complementary laser approaches are explored today. First, thanks to the advent of novel intense laser sources in the infrared range (nanosecond and femtosecond lasers), internal modification of silicon has become possible, as reviewed by Chambonneau et al.[6] However, the specificities of nonlinear interactions in semiconductors lead to situations much more challenging than in dielectrics for waveguide writing and index engineering. In practice, proof-of-concept 3D writing demonstrations in silicon rely on unconventional strategies[7] and efforts today concentrate on finding practical solutions for applications. The second approach covered by this paper relies on

M. Garcia-Lechuga, N. Casquero, J. Siegel, J. Solis
Laser Processing Group, Instituto de Optica Daza de Valdes (IO) CSIC
Madrid 28006, Spain
E-mail: mario.garcia.lechuga@csic.es
R. Clady, A. Wang, O. Utéza, D. Grojo
Aix Marseille Université
CNRS, LP3, UMR7341
Marseille 13288, France

The ORCID identification number(s) for the author(s) of this article can be found under https://doi.org/10.1002/lpor.202301327

DOI: 10.1002/lpor.202301327

surface processing. Laser melting/annealing is a well-established technique for enabling surface re-crystallization of amorphous silicon using pulsed lasers in nanosecond or longer regimes.[8] The reverse process of amorphization of crystalline silicon is also possible when intense picosecond and femtosecond lasers are used.[9] In this case, it is the extremely rapid cooling conditions after melting which prevents material recrystallization.[10] For applications, high-resolution writing of amorphous-crystalline elements has been demonstrated by applying strong focusing conditions[11,12] or relying on the spontaneous formation of periodic sub-wavelength structures.[13,14]

The significance of this controllable amorphization process in silicon photonics is evident in its potential to create surface waveguides. This interest arises from the higher refractive index ($\Delta n = 6.2 \cdot 10^{-2}$[15]) of the amorphous phase in comparison to the crystalline phase, as well as the transparency of both phases in the telecom range. The challenge is then to achieve a sufficient thickness of the amorphous layer ($d_{\text{a-Si}}$) to satisfy waveguiding conditions. In this context, recent advances have shown that it is possible to surpass the previously reported limit at $d_{\text{a-Si}} = 60$ nm[16–20] and capabilities are today extended beyond $d_{\text{a-Si}} = 120$ nm.[21] This progress has been achieved with the introduction of mid-infrared radiation and the implementation of a dielectric cover layer for faster heat extraction. While such recent success is very interesting, they also indicate that there is very likely room for improvements by exploring new strategies using ultrashort laser pulses.

In this context, there are still important open questions on the underlying physical processes and more experimental parameters to explore. In particular, it is extremely important to understand the aspects that define the "fluence window" in which amorphization is obtained. As demonstrated by Bonse's group[16,20,22] and in our previous work,[21] experiments with single pulses and Gaussian beam focus lead to thickness profiles for the amorphous layer that are nearly proportional to the applied local fluence. The reach of larger depths is truncated and made inaccessible at higher fluences due to the thresholds for other physical phenomena such as ablation or recrystallization. In this regard, Florian et al.[20] recently showed, for irradiations at $\lambda = 800$ nm wavelength and $\tau = 30$ fs pulse duration, that the fluence window for amorphization in Si(111) was larger than the one for Si(100), leading to a maximum amorphization thickness of $d_{\text{a-Si}} = 50$ nm for Si(111) compared to only $d_{\text{a-Si}} = 25$ nm for Si(100). In practice, amorphization of Si(111) was limited by ablation and Si(100) by recrystallization. This is consistent with the faster epitaxial recrystallization velocity known for the (100) crystal orientation.[23,24] In simplified descriptions, amorphization and ablation can be primarily associated with the delivery of sufficient energy to overcome the melting or boiling temperature ($T_M = 1687$ K and $T_B = 3538$ K, respectively). However, it is important to note that recrystallization is a multi-parameter dynamical process making it difficult to express similarly simple threshold conditions for its occurrence.

The objective here is a comprehensive report on the modification limits, specifically the amorphization fluence range and maximum amorphization depth, by scrutinizing the modification morphologies generated by state-of-the-art femtosecond laser technologies. The work is organized as follows.

In Section 2, an exhaustive literature overview of amorphization fluence thresholds and ablation fluence thresholds is presented, considering all tested pulse durations at $\lambda = 800$ nm (the most common wavelength) and spectral dependencies compiling data from studies using wavelengths ranging from UV to mid-infrared (MIR). An important discussion concerns the trends observed with these control parameters as well as the gaps existing in the literature data. Section 3 concentrates on experimental results obtained by our group and is divided into three subsections. Subsection 3.1 describes the applied criteria for transformation threshold determination using optical microscopy (OM) and atomic force microscopy (AFM). Additionally, a correlation between transient melting and permanent amorphization is demonstrated based on time-resolved microscopy measurements. In Subsection 3.2, we describe the results of a study performed on Si(111) at $\lambda = 800$ nm as a function of pulse duration in the ultrashort single-shot regime, from $\tau = 13.9$ to 134 fs. The measured fluence threshold values (amorphization and ablation) are compared with the experimental and theoretical data in the literature. This extends the knowledge of the transformation thresholds to pulses shorter than $\tau = 30$ fs. Additionally, this work provides the first complete analysis of the maximum achievable amorphization depth as a function of the pulse duration. In Subsection 3.3, complementary to a previous report on dielectrics,[25] we present a complete set of new data on the role of the laser wavelength for Si processing. This covers irradiation wavelengths from $\lambda = 258$ to 4000 nm $\approx \tau = 200$ fs). Experiments are conducted on Si(111) and Si(100) samples, revealing notable differences in amorphization thicknesses at specific wavelengths and unexpected similarities at others. Finally, in Subsection 3.4, For the infrared domain, in which the triggered nonlinear absorption processes influence the achievable transformation depths, we also discuss the question of the spatial resolution for writing. After a rigorous mapping between laser modifications and the experimentally characterized 2D beam profile, it is confirmed that the strict threshold-based responses make it impossible to benefit from the concept of nonlinear resolution, as recently demonstrated for dielectrics.[26] Finally, in Section 4, we summarize the main conclusions, while the "Experimental Section" is presented in Section 5.

2. Review of Modification Thresholds in Silicon Under Ultrashort Pulse Irradiations

2.1. Influence of the Pulse Duration Irradiations at $\lambda = 800$ nm

The long-established maturity of Ti:Sapphire laser technology leads to studies in the ultrafast regime, which were often conducted at $\lambda = 800$ nm. Compiling various reports from the scientific literature, **Figure 1** presents an extended dataset on the thresholds for silicon modifications as measured by many groups worldwide at $\lambda = 800$ nm. To extract the influence of the pulse duration, the thresholds are presented as a function of this parameter and we mainly compare results obtained from single-shot irradiation experiments. Efforts have been also made to convert all available data in a unified frame (expressing all results in terms of peak fluence $F_0 = 2E/\pi w_0^2$, where E and w_0 denotes the pulse energy and beam radius at $1/e^2$ respectively) to ensure reliable

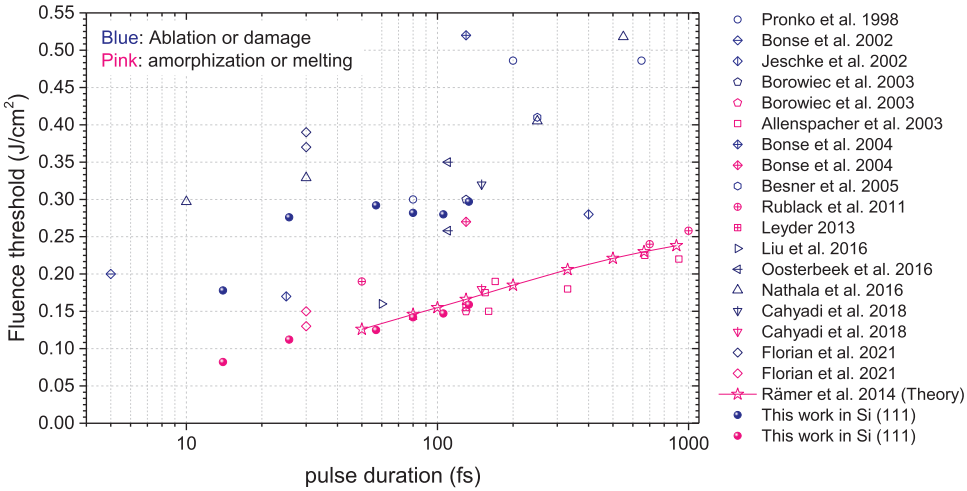

Figure 1. Laser-induced modification thresholds of silicon surfaces, reported by different groups using pulses of different pulse durations at $\lambda = 800$ nm. Experimental data are extracted from[20,27,36–38,28–35] and all correspond to single-shot irradiation experiments except,[36,37] where the studies extend to some incubation processes (see Table S1, Supporting Information for details). Data from calculations are extracted from.[39] For comparison and to facilitate the discussions in Subsection 3.2, the dataset also includes our experimental measurements obtained for Si(111).

comparisons. The information presented in Figure 1 is complemented by Table S1 (Supporting Information), which provides additional details regarding the studied materials, the laser conditions, and the applied methodologies for the analyses.

In various studies, modifications are categorized as melting, amorphization, damage, or ablation. In the presentation of the threshold data shown in Figure 1 (more details in Table S1, Supporting Information), we have grouped the works referring to melting and amorphization, represented by pink symbols. In Subsection 3.1.2., we will show that this grouping can be justified by experiments revealing an excellent correlation between melting and amorphization thresholds. The same grouping approach is applied to the data for damage and ablation (blue symbols). However, it should be pointed out that some authors associate melting and damage, for example, the work by Allenspacher et al.[31] In these cases, we have categorized the measurements as for melting rather than damage. The relatively clear spatial separation of the amorphization and ablation regimes (magenta and blue) directly supports our grouping and categorization approach. Remarkably, despite a compilation based on works from more than ten research groups over three decades and, consequently, a large variety of laser sources, materials, and conditions used for these works, the two sets of threshold data ($F_{\mathrm{th,Am}}$ and $F_{\mathrm{th,Ab}}$) reveal relatively clear trends over the full sub-picosecond domain. This offers a rather complete quantitative presentation of the required laser conditions for silicon modifications in the ultrashort temporal regime.

The agreement between studies is particularly pronounced for the amorphization fluence thresholds, even valid across a wide range of studied conditions. The considered works highlight that the amorphization threshold exhibits modest sensitivity to crystal orientations (see Florian et al.[20]), doping levels (see Leyder[34]), or the presence of dielectric cover layers (see Rublack et al.[33]). Interestingly, we also integrate into our compilation simulations obtained by Rämer et al.[39] (see the star symbols in Figure 1), covering a large range of pulse durations ($\tau = 50$ fs to 6 ps). The modeling approach based on the density-dependent two-temperature model (nTTM)[40] accounts for all processes (energy absorption including linear and two-photon absorption, relaxation, and transport) taking place during and after laser-matter interaction. It is then expected to provide an accurate description of the evolution of silicon conditions up to its transformation threshold. In this work,[39] it is important to emphasize that the modification is associated with the melting temperature of silicon, which is used as a criterion for threshold determination. This is totally consistent with our grouping approach. Moreover, the authors underline that important transient optical material properties (transient carrier collision frequency in the description of the Drude model) should be incorporated in the modeling for good accuracy, while transport and degeneracy effects can be neglected. While numerous other modeling and simulation studies on ultrafast laser processing studies can be found in the literature, we have chosen this modeling work for presentation in Figure 1 because it appears in excellent agreement with the collected set of experimental data within the full studied temporal range. Nevertheless, Figure 1 also shows that data is scarcer for the shortest pulses. The regime with pulse duration shorter than $\tau = 50$ fs was to date exclusively covered by the recent work by Florian et al.[20] ($\tau = 30$ fs). These aspects represent a strong motivation for our additional experimental study, presented later in this paper to fill this gap (Subsection 3.2) and complement and confirm the available dataset.

For ablation or damage, more reports can be found, including the pioneer's work by Pronko et al.[27] exploring different pulse durations and the one by Bonse et al.[28] reporting measurements with of $\tau = 5$ fs. Additionally, Besner et al.[32] explored the influence of ambient medium, reporting similar values for vacuum conditions, air, or immersion in water. We note a much larger dispersion of the available data gathered in Figure 1. While a trend is observed, we conclude from the literature a less predictable situation that can be attributed to laser conditions being more difficult to characterize, more subjective observables, or different criteria

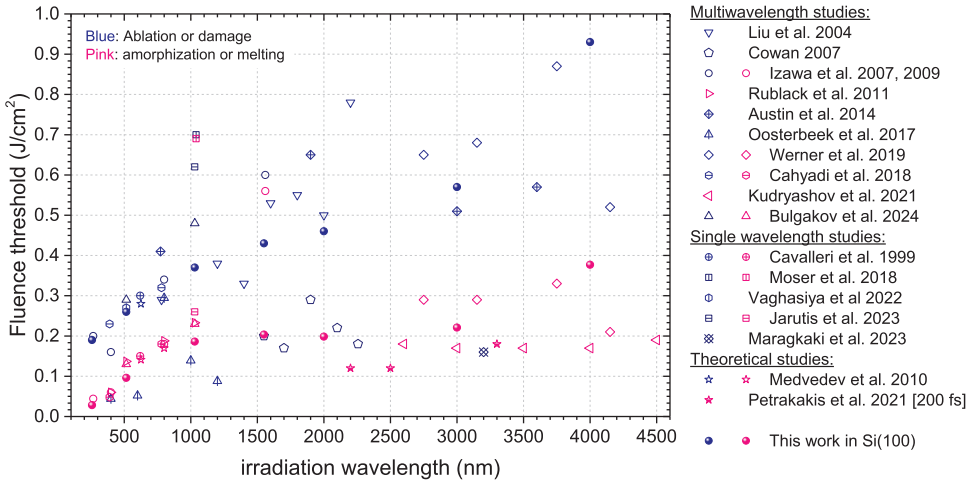

Figure 2. The laser-induced modification thresholds of silicon surfaces, as reported by various groups using ultrashort pulses at different irradiation wavelengths. Experimental data are extracted from [17,19,55–57,38,43–47,49,50] and combined with theoretical calculations extracted from.[58,59] The pulse duration in the considered reports varies from $\tau = 45$ fs up to $\tau = 1.1$ ps (see Table S2, Supporting Information for details). For comparison and to facilitate the discussions in Subsection 3.3, the dataset also includes our experimental measurements for Si(100).

used for ablation detection (see Table S1, Supporting Information for details on the criteria used on the different references).

2.2. Influence of the Irradiation Wavelength

Besides the vast number of publications describing works using Ti:sapphire-based laser systems operating at $\lambda = 800$ nm, results in other wavelength ranges are available and more are progressively coming with the advent of new and diverse ultrafast laser technologies.

Particularly in the 1990's, fluence thresholds for silicon melting were reported using dye lasers ($\lambda \approx 620$ nm) as reviewed by Korfiatis et al..[41] Another routinely accessible wavelength range is the one around $\lambda = 1050$ nm as it corresponds to Yb-doped crystal or fiber laser technologies. With this condition, the number of works is less than those at $\lambda = 800$ nm, but still considerable, including studies on the role of the pulse duration[27,42] or crystal orientation and doping.[43]

Other spectral regions, from the ultraviolet to the mid-infrared, are accessible through non-linear processes, such as harmonic generation (HG) or optical parametric amplification (OPA). While few in number, the reports on multi-wavelength studies of ultrafast laser modification of silicon are valuable to reference at this stage. Liu et al.[44] report fluence threshold values for ablation from $\lambda = 780$ to 2200 nm. Cowan[45] gives values for damage from $\lambda = 1550$ to 2556 nm. From Izawa et al.,[17,46] one can extract threshold values for amorphization and ablation from $\lambda = 258$ to 1560 nm, and from Rublack et al.[33] threshold values for melting, ablation, and dielectric thin-film removal from $\lambda = 400$ to 1030 nm. The group of Chowdhury[19,47] provides threshold values for ablation from $\lambda = 773$ to 4150 nm and for melting from $\lambda = 2750$ to 4150 nm. Gallais et al.[48] measure fluence thresholds for ablation from $\lambda = 310$ to 1030 nm and Oosterbeek et al.[49] from $\lambda = 400$ to 1200 nm. Finally, Kudryashov et al.[50] concentrate on the mid-infrared domain, giving damage threshold values (corresponding to amorphization in this work) from $\lambda = 2600$ to 4500 nm.

In **Figure 2**, we present the fluence threshold values considered as the most relevant and originating from comparable studies in order to assess the role of the laser wavelength (see Table S2, Supporting Information for details). Our selection is based on the following considerations. First, we consider only reports using sub-picosecond pulses, excluding the important works by Thorstensen et al.[51] and Sikora et al.[52] covering various wavelengths ($\lambda = 343$, 515, and 1030 nm) but concentrating on the picosecond regime ($\tau = 3$ and $\tau = 50$ ps, respectively). The interesting work conducted at $\lambda = 5100$ nm by Agustsson et al.[53] is also excluded for the same reason ($\tau = 5$ ps). Second, all the previously mentioned reports on multiwavelength studies are included, except for the work of Gallais et al..[48] According to the authors, their data are not directly comparable to the other published works unless a rescaling factor is applied. Additionally, two works reporting threshold values at two different wavelengths are also accounted for, as the work by Cahyadi et al.[38] at $\lambda = 390$ and 780 nm and the one by Bulgakov et al.[54] at $\lambda = 515$ and 1030 nm. Third, for single-wavelength studies, we decided to consider only works where both the fluence threshold for ablation and for melting or amorphization were provided. Among these, we have prioritized studies conducted at wavelengths not covered by other research.

In Figure 2, as done for Figure 1, results from theoretical works have also been included. These correspond to: i) the work by Medvedev et al.[59] for visible wavelengths and accounting for linear and two-photon absorption, and ii) the simulations by Petrakakis et al.[58] for the infrared domain ($\lambda = 2200$, 2500, and 3300 nm) and accordingly accounting for two-photon and three-photon absorption processes. Both studies use the condition for melting as the criterion that defines the damage threshold. Additionally, Medvedev et al.[59] associate the conditions for optical breakdown with the occurrence of material ablation at $\lambda = 625$ nm.

At first glance, Figure 2 reveals a relatively large dispersion of the available data. To facilitate the general visualization of specific trends, we have also added on the same graphs our measurements obtained for Si(100) (details and discussions in Subsection 3.3). From all the data, one can note a noticeable gap between the amorphization (pink color) and ablation threshold values (blue color), despite some exceptions that will be simply omitted in the discussions. For amorphization, those excluded data are the ones from Moser et al.[57] (at $\lambda = 1040$ nm) and from Izawa et al.[17] (at $\lambda = 1560$ nm) which correspond to threshold values significantly higher than the rest and very close to the ablation threshold. For ablation, the excluded studies are those from Oosterbeek et al.,[49] Cowan,[45] and Maragkaki et al.[60] which tend to minimize the apparent threshold values due to experiments conducted with multipulse irradiation (incubation) conditions (see Table S2, Supporting Information for details).

Regarding the evolution of the fluence threshold of amorphization as a function of the irradiation wavelength, an increase from UV to near-infrared (NIR) wavelengths ($\lambda < 1100$ nm) for amorphization is observed, with values ranging from 0.04 to 0.26 J cm^{-2}. It is important to note that this change in threshold observed when tuning the irradiation wavelength (a 550% increase) is significantly larger than when varying the pulse duration (for example, a 33% increase from $\tau = 100$ to 330 fs, as reported by Rämer et al.[39] at $\lambda = 800$ nm). In the transparency domain of silicon ($\lambda > 1100$ nm), there is a lack of information from $\lambda = 1100$ to 2500 nm, which is one of the motivations for our additional measurements presented in Subsection 3.3. Above $\lambda = 2500$ nm, the fluence thresholds for amorphization as determined by Werner et al.[19] and Kudryashov et al.[50] are almost wavelength-independent. In practice, the observed variations in the reported threshold values can be attributed to some other experimental parameters that may vary in the different studies, such as the angle of incidence or the pulse duration (see Table S2, Supporting Information for details).

Concentrating on the trends for measured fluence thresholds of ablation as a function of the irradiation wavelength, a linear increase in the spectral range from UV to NIR can be observed The threshold values increase from typically 0.2 to ≈0.5 J cm^{-2} (an increase of 150%). However, due to the limited and highly dispersed data reported in the spectral region from NIR to MIR by Liu et al.[44] and Chowdhury's group,[19,47] a quantitative analysis becomes impossible. This underscores the necessity for further studies to determine the fluence threshold of ablation in this spectral regime.

Finally, although it is out of the scope of our report, it remains interesting to comment on a few other studies of silicon modification using free electron lasers and so extreme UV radiation. Stojanovic et al.[61] report on a fluence threshold for melting at 100 mJ cm^{-2} and a threshold for ablation at 380 mJ cm^{-2} for a wavelength of $\lambda = 32.5$ nm ($\tau = 25$ fs). Dinh et al.[62] report on an ablation threshold at 418 and 106 mJ cm^{-2} for wavelengths of $\tau = 13.5$ and 10.3 nm ($\tau = 70$ fs). None of those values confirms a continuously vanishing threshold when decreasing the wavelength as observed in Figure 2. This probably indicates completely different interaction regimes when very short wavelengths come into play.

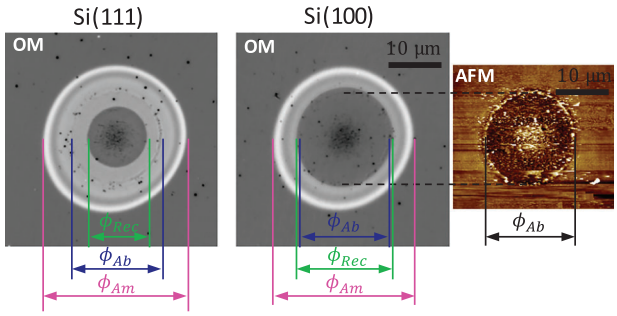

Figure 3. (Left and center) Optical microscope images of single-shot laser-induced modifications under $\lambda = 4000$ nm in Si(111) (n-type. 0.002-0.005 Ω·cm) and Si(100) (intrinsic. 200–600 Ω·cm) as recorded with an illumination at $\lambda_{LED} = 460$ nm. The irradiation peak fluence is $F_0 = 1.44$ J cm^{-2}. Different types of modifications, including recrystallization (Rec), ablation (Ab), and amorphization (Am), and their corresponding diameters, ϕ, are shown. (Right) Atomic force microscopy image of the same modified spot in Si(100).

3. Results and Discussions

3.1. Identifying the Silicon Transformation Thresholds

3.1.1. Amorphization, Ablation, and Recrystallization

Any thorough investigation of transformation thresholds for silicon or other semiconductors requires a precise definition of the corresponding transformations. For reliable comparisons, it also needs rigorous and systematic experimental methods and criteria to determine them. One of the most detailed morphological studies of silicon under single-shot femtosecond irradiations is the research by Bonse's group.[16,20,22,28] In their research, laser-induced amorphization is characterized via optical microscopy (OM), Raman spectroscopy, or spectroscopic imaging ellipsometry. For the case of the ablation threshold, the characterization includes optical microscopy, scanning electron microscopy (SEM), and atomic force microscopy (AFM).

In order to clarify and also show our determination criteria for the different transformation thresholds for silicon, **Figure 3** presents optical microscopy images and an AFM image of features produced by single-pulse irradiation of Si(111) (n-type. 0.002–0.005 Ω·cm) and Si(100) (intrinsic. 200–600 Ω·cm) surfaces. The full experimental procedure for obtaining these transformations is explained in detail in Subsection 5.3. In particular, in this case, we make use of pulses at $\lambda = 4000$ nm and $\tau = 190$ fs, focused on a Gaussian spot diameter (at $1/e^2$ the intensity peak) of $2w_0 = 31.0$ μm, with a selected peak fluence of $F_0 = 1.44$ J cm^{-2}.

First, the ablation crater with a diameter ϕ_{Ab} can be identified by a smooth change of reflectivity in the OM images (limits noted by blue lines in Figure 3) and matches the diameter measured in the corresponding AFM image, providing quantitative insight into the surface topography. Second, for localizing the amorphization limits, the most established method is OM due to the very different optical properties of the crystalline and amorphous phases of silicon.[16,18,22] Amorphous layers have a higher reflectivity than the crystalline phase throughout the visible and

NIR regions of the spectrum. This fact can be directly appreciated in the OM images of Figure 3 (limits noted by pink lines), in which the entire region of enhanced reflectivity corresponds to the amorphous phase with a corresponding apparent diameter ϕ_{Am}.

Third, another type of transformation that can be observed is recrystallization. This process typically occurs at high fluence levels (always above the $F_{th,am}$), leading to a situation in which a high amount of deposited energy cannot be extracted sufficiently fast to allow amorphization. Very little work has been reported on the threshold conditions for this process. In Figure 3, this transformation corresponds to the situation where the reflectivity becomes equal to that of the pristine material (limits indicated by green lines). For Si(111), this limit occurs at fluences above the ablation threshold, but for Si(100), occurs close below. Therefore, this limit remains a crucial aspect, since it may define the upper boundary for the laser processing window in the amorphization regime. As will be demonstrated throughout this article, the upper fluence limit for amorphization, whether caused by recrystallization or ablation, depends on the situation (irradiation conditions and/or crystalline orientation of the sample).

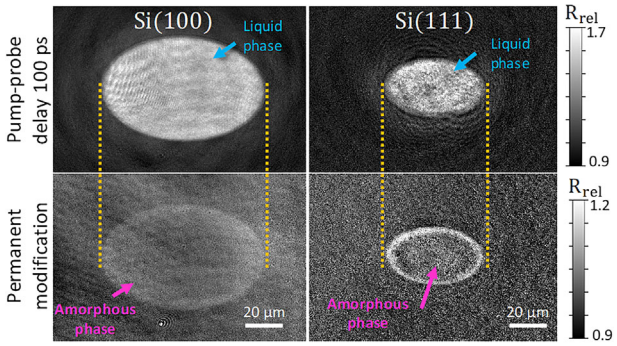

Figure 4. (Top) Time-resolved microscopy images at a delay of 100 ps between the pump pulse ($\lambda = 800$ nm, $\tau = 120$ fs) and the probe pulse ($\lambda = 400$ nm, $\tau \approx 100$ fs) on the surface of silicon. (Bottom) Optical microscopy images (illumination at $\lambda = 400$ nm) of permanent modifications induced in silicon. The irradiation conditions are single-pulse, angle of incidence of 52°, p-polarized light, and peak irradiation fluence of 244 and 255 mJ cm^{-2} respectively for Si(100) and Si(111). Yellow vertical lines are a guide to the eye to compare the lateral extension of transient melting (Top) and permanent amorphization (Bottom). The different modification sizes between Si(100) and Si(111) correspond to the use of different focusing conditions (different spot sizes).

3.1.2. Melting Threshold or Amorphization Threshold

In addition to the three types of transformations described above (ablation, amorphization, and recrystallization), there is another transient transformation state: the melt phase, which occurs just after the irradiation. The determination of its threshold is far more challenging since the post-mortem inspection with the above methods does not necessarily exhibit changes directly indicative of melting. The concept of non-thermal melting discussed for ultrafast strong field interactions can also lead to complications in interpretations. A widespread simplification is often made to circumvent this problem in crystalline semiconductors. It consists in associating amorphization as a signature of melting conditions. This is in line with the vision that melting caused by ultrashort pulses is inevitably followed by rapid quenching conditions such that the atoms cannot arrange fast enough to recover the crystal structure.[63]

While this simplification seems to be generally accepted by the community, it does not rigorously hold for many cases in which the material recovers the crystalline phase, such as femtosecond laser irradiation at $\lambda = 800$ nm of germanium[64] or irradiations with much longer laser pulses. The measurement of a short-lived event such as melting requires the use of time-resolved techniques. In particular, this can be done using time-resolved optical probe techniques that exploit the fact that the optical properties of the molten phase differ strongly from those of the solid phases (crystalline and amorphous, each with their characteristic properties).[65]

While numerous works have employed these techniques to determine the melting threshold of semiconductors and metals,[66–69] to the best of our knowledge, very few have rigorously correlated amorphization and time-resolved measurements in order to confirm corresponding thresholds. To this end, we have performed pump-and-probe femtosecond microscopy (see Subsection 5.1 for method details) investigations in Si(100) and Si(111). The applied technique records reflectivity snapshots of the laser-excited region using an ultrashort probe pulse for illumination.[65] The same experimental arrangement has thus the ability to record images of the material in both states: the molten phase and the final amorphous phase.[12,70]

Figure 4 shows the results obtained with single-pulse irradiations at $\lambda = 800$ nm and $\tau = 120$ fs. The ellipticity of the spots is due to the angle of incidence of the pump pulse (52°) while the probe pulse illuminates the sample at normal incidence. The delay value chosen to probe the final amorphous phase exceeds several seconds after irradiation to ensure the probing of the resolidified and cooled material. In both cases, the lateral extension of the amorphous phase can be precisely determined since it is accompanied by an increase in reflectivity.[16,18,22] The delay chosen is 100 ps in order to determine the maximum extension of the molten phase. This delay is long enough to enable the generation of a dense free electron plasma, flowed by electron-phonon coupling and heat flow within the molten region. This delay is also sufficiently short to probe the transient state before the resolidification is initiated. A comparison of the lateral extensions of the laser-amorphized and the molten regions in Figure 4 immediately reveals that they are very similar for both crystal orientations of Si. From these 4 images, we can quantify the threshold values using the local-fluence method.

The determined fluence thresholds for melting of Si(100) and Si(111) are identical (148 ± 4 mJ cm^{-2}). This is consistent with physical and optical properties independent of crystal orientation. Also, the values obtained for amorphization agree for both crystal orientations (147 ± 4 mJ cm^{-2}). However, the most important conclusion for the present discussion is that the amorphization and melting thresholds are measured to be identical, with a maximum uncertainty of 2%. These results confirm that indeed, at least for this combination of pulse duration and laser wavelength, the determination of the melting threshold can be reliably done by inspection of the laser-amorphized regions.

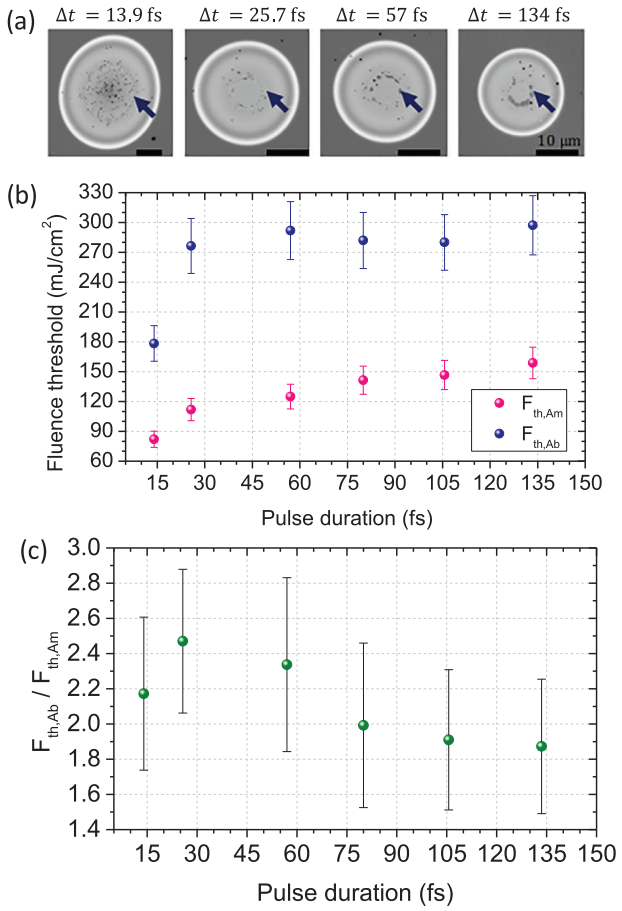

Figure 5. a) Optical microscopy images of laser-induced modifications at $\lambda = 800$ nm and different pulse durations in Si(111) were recorded with illumination at $\lambda_{LED} = 460$ nm. The modifications correspond to single-pulse irradiations performed above the fluence threshold for ablation. (F_0 ($\tau = 13.9$ fs) = 222 mJ cm^{-2}; F_0 ($\tau = 25.7$ fs) = 297 mJ cm^{-2}; F_0 ($\tau = 57$ fs) = 314 mJ cm^{-2}; F_0 ($\tau = 134$ fs) = 314 mJ cm^{-2}). The blue arrow indicates the ablation feature. The image contrast (greyscale) is set to display the reflectivity in the range [0.8, 1.3] and the scale bars correspond to 10 μm. b) Amorphization (pink) and ablation (blue) fluence threshold as a function of the femtosecond pulse duration. c) Ratio of ablation and amorphization fluence thresholds.

3.2. Results with Different Pulse Durations ($\lambda = 800$ nm): from $\tau = 13.9$ to 134 fs

3.2.1. Fluence Thresholds for Amorphization and Ablation as a Function of Pulse Duration

The experimental procedure for this work aiming at complementing the available data is explained in Subsection 5.2. In **Figure 5a**, images of modified spots created with different pulse durations are shown. The outer border of the modification illustrates the amorphization limit, while the arrow indicates the ablation feature. Following the methodology for retrieving the fluence threshold values explained in Subsection 5.4, **Table 1**, and Figure 5b, we present the measured fluence threshold values for amorphization and ablation using different pulse durations from $\tau = 13.9$ to 134 fs (at full-width half maximum – FWHM).

Table 1. Pulse-duration dependent fluence thresholds for ablation and amorphization in Si(111) (n-doped, 0.002 – 0.005 ohm·cm) at $\lambda = 800$ nm. The error on the determined fluence thresholds is estimated at 10% (see text). The uncertainties associated with the waist values correspond to errors derived from the application of Liu's method (D^2-method).

τ [fs]	$F_{th,Am}$ [mJ cm^{-2}]	$F_{th,Ab}$ [mJ cm^{-2}]	w_0 (1/e^2 [μm])
13.9 fs	82 ± 8	178 ± 18	30.1 ± 0.7
25.7 fs	111 ± 11	280 ± 30	18.52 ± 0.14
57 fs	125 ± 13	290 ± 30	18.6 ± 0.2
80 fs	141 ± 14	280 ± 30	19.1 ± 0.2
106 fs	147 ± 15	280 ± 30	19.0 ± 0.2
134 fs	160 ± 16	300 ± 30	18.57 ± 0.12

By analyzing these new data (Figure 5b) and comparing them with previous experimental works and the theoretical calculations by Rämer et al.[39] (see Figure 1), we can immediately confirm a good agreement for pulse durations longer than $\tau = 50$ fs. Additionally, we experimentally confirm the progressive decrease of the amorphization (melting) fluence threshold with the reduction of pulse duration. Based on the two most extreme values from our work (with $F_{th,Am} = 160$ mJ cm^{-2} for $\tau = 134$ fs and 82 mJ cm^{-2} for $\tau = 13.9$ fs), there is a twofold decrease in the applied fluence required to reach melting/amorphization.

Similarly to dielectric studies,[71–74] the higher probability of photoionization at high intensity can explain the observed reduction in the modification threshold of silicon with pulse shortening. Despite the existence of linear absorption in this spectral range for silicon, the dominance of nonlinear absorption becomes possible, given that single-photon absorption is indirect (requiring also momentum change) and nonlinear absorption may arise from a direct transition path.[40]

Regarding the obtained values for the ablation threshold ($F_{th,Ab}$), a decrease is also found for the shortest pulse duration ($\tau = 13.9$ fs). However, for higher pulse durations, a situation rather insensitive to this laser parameter is revealed. Relatively constant ablation threshold values, within the range of $F_{th,Ab} = 270$ to 300 mJ cm^{-2}, are measured with pulse durations from $\tau = 25.7$ to 134 fs. The ratio between ablation and amorphization thresholds ($F_{th,Ab}$ / $F_{th,Am}$) is represented in Figure 5c, indicating a factor of ≈2 for all cases. Even if variations are in the range of the error bar, an interesting conclusion from this presentation is about the fluence "window" for amorphization, which tends to become slightly narrower with increasing pulse durations.

3.2.2. Maximum Amorphization Depth as a Function of the Pulse Duration

The fact that the optical properties of the amorphous phase differ strongly from those of the crystalline phase is exploited to detect the amorphization threshold by means of optical microscopy. In addition, the optical microscopy images also contain information about the thickness of the produced amorphous layer since the absorption coefficient of the amorphous phase in the visible and infrared region is sufficiently low to allow contributions in the image from the light reflected from the embedded

crystalline/amorphous interface. With monochromatic illumination, this light interferes with the component reflected at the amorphous/air interface. Such thin-film interferometric imaging configuration leads to images of laser-amorphized regions that exhibit annular ring structures, in which the number of rings increases with the thickness of the amorphous surface layer. This method has been widely used to determine the maximum achievable thickness of amorphous layers[16,21] and to reconstruct cross-sectional views of laser-induced periodic amorphous surface structures.[18] More details on the methodology are given in Subsection 5.5. Similarly to the case of fs-resolved imaging (see Subsection 3.1.2), the 2D information contained in the reflectivity images of the surface after irradiation can also be used to acquire direct information regarding the fluence dependence of the transformation with prior knowledge of the beam waist.

To determine the maximum achievable amorphization thickness, one should approach the fluence threshold for ablation, which is defined as the limiting factor for Si(111). To illustrate how to determine this limit, we show in **Figure 6a** two modifications produced under pulses with a duration of $\tau = 13.9$ fs: at the highest available peak fluence below the ablation threshold ($F_0 = 158$ mJ cm^{-2}) and at the lowest available fluence above the ablation threshold ($F_0 = 188$ mJ cm^{-2}). It should be mentioned that with our experimental configuration for energy attenuation (see Subsection 5.3 and reference[25]) we cannot access intermediate peak fluences between the two shown discrete fluence levels. A radial analysis of the modification image produced at $F_0 = 188$ mJ cm^{-2} is shown in Figure 6c, after converting the spatial coordinates (x-axis) into local fluences. The ablation signature can be identified, indicating the upper fluence limit for amorphization. Together with this curve, Figure 6c presents the reflectivity profiles extracted from the modification images produced under pulses with durations of $\tau = 25.7$, 57, 80, 106, and 134 fs (shown in Figure. 6b. Plotting together in Figure 6d the reflectivity values at the highest fluence and the calculated reflectivity behavior of an amorphous layer on the top of a crystalline bulk (see Subsection 5.5) enables deriving the maximum amorphization depth reached in each case. Figure 6e represents the amorphization depth versus the pulse duration, observing that independently of the pulse duration (covering from $\tau = 13.9$ to 134 fs) a mostly unchanged maximum layer thickness of $d_{a\text{-}Si} = 80$ nm is obtained. The very modest variation with slightly thinner amorphization thickness for longer pulses, as shown in Figure 6e, can be directly associated with the previously noticed trend on the fluence window for amorphization, as the latter also tends to decrease (see Subsection 3.2.1).

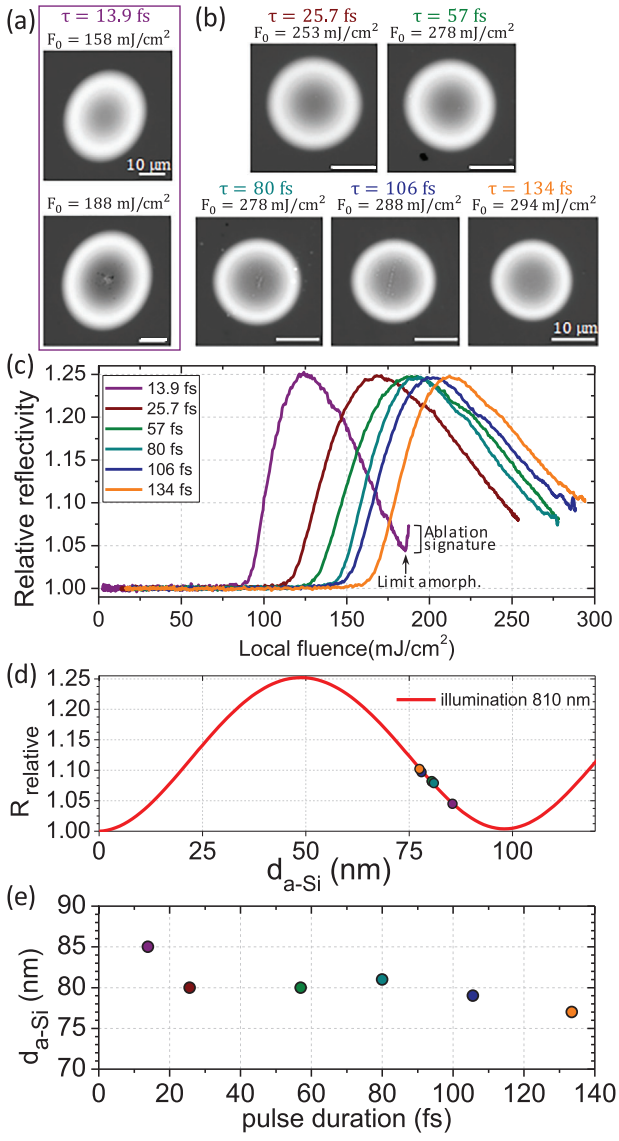

Figure 6. a,b) Optical microscope images (illumination at $\lambda_{LED} = 810$ nm) of laser-induced modifications in Si(111) obtained with single-pulse irradiations using different pulse durations. a) Modifications by pulses of $\tau = 13.9$ fs at peak fluences close below and close above the ablation threshold. b) Modifications at peak fluences close below the ablation threshold for different pulse durations. c) Reflectivity profiles extracted by radial analysis of imaged spots shown in (a) (bottom) and (b). d) Calculated relative reflectivity evolution as a function of amorphous layer thickness ($d_{a\text{-}Si}$) under illumination at $\lambda_{LED} = 810$ nm (see Subsection 5.5). Circles correspond to the experimental reflectivity values at the highest fluence for profiles shown in (c) (except for $\tau = 13.9$ fs, using the limit of amorphization). The color code is the same as for lines in (c). e) Amorphous layer thickness as a function of the pulse duration extracted from the radial analyses (c) and the reflectivity calculations (d).

3.3. Results with Different Wavelengths: from $\lambda = 258$ to 4000 nm

3.3.1. Fluence Thresholds for Amorphization and Ablation as a Function of Irradiation Wavelength

In this subsection, we present measured fluence threshold values for amorphization and ablation (see **Figure 7**, **Table 2**, and Table S3, Supporting Information) after performing experiments using different irradiation wavelengths. Figure 7 summarizes the obtained results, covering a large spectral range from ultraviolet ($\lambda = 258$ nm) to mid-infrared ($\lambda = 4000$ nm). The experimental procedure for these multi-wavelength studies is explained in Subsection 5.3, and the methodology for retrieving the fluence threshold values (illustrated by an example at $\lambda = 4000$ nm) can be found in Subsection 5.4. The reported data rely on two

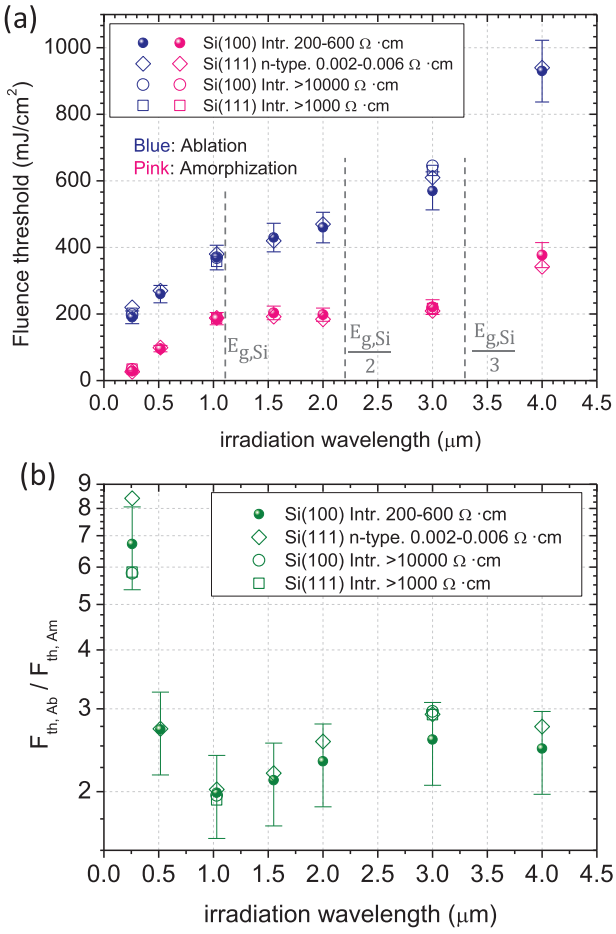

Figure 7. a) Fluence thresholds for amorphization (in pink) and ablation (in blue) as a function of the irradiation wavelength of various silicon samples. Pulse durations are $\tau \cong$ 200 fs for all considered wavelengths. Dashed lines represent the photon energies corresponding to the material bandgap ($E_{g,Si}$) and submultiples in order to indicate the regions of linear absorption and nonlinear absorption. b) The ratio between the obtained threshold values (ablation and amorphization). Error bars are only included for Si(100) intrinsic 200–600 Ω·cm for clearer visualization, but similar bars apply to the other three samples.

Table 2. Wavelength-dependent fluence threshold values for ablation ($F_{th,Ab}$) and amorphization ($F_{th,Am}$) in Si(100) (intrinsic. 200–600 Ω·cm) and laser waist (w_0) values. The error on the fluence threshold values is estimated at 10%, as detailed in Subsection 5.4. The uncertainties associated with the waist values correspond to errors derived from the application of Liu's method (D^2-method).[75,76]. Details and data for the other investigated samples can be found in Table S3 (Supporting Information).

λ [nm]	$F_{th,Am}$ [mJ cm^{-2}]	$F_{th,Ab}$ [mJ cm^{-2}]	w_0 (1/e^2) [μm]
258	28 ± 3	190 ± 19	6.57 ± 0.05
515	96 ± 10	260 ± 30	10.01 ± 0.08
1030	186 ± 19	370 ± 40	17.6 ± 0.3
1550	200 ± 20	430 ± 40	16.84 ± 0.07
2000	200 ± 20	460 ± 50	15.00 ± 0.09
3000	220 ± 20	570 ± 60	15.9 ± 0.4
4000	380 ± 40	930 ± 90	15.50 ± 0.12

experimental campaigns. The first campaign covered 7 different wavelengths: 258, 515, 1030, 1550, 2000, 3000, and 4000 nm. The second campaign covered 3 well-separated wavelengths: 258, 1030, and 3000 nm. In this latter case, larger spot sizes were applied (see Table S3, Supporting Information), and particular attention was paid to comparing only intrinsic samples for both Si(100) and Si(111).

Figure 7a reveals two significant observations right away. First, the differences in fluence threshold values between Si(100) and Si(111) are very small, when not null. The most notable difference between the two orientations is observed at λ = 4000 nm (12% higher amorphization threshold for Si(100)). This difference can be visually checked in Subsection 5.4. Second, the level of doping appears to have no significant effect on the fluence threshold values, as illustrated by the measurements on the two Si(111) samples, which exhibit significantly different resistivity values compared to the two Si(100) samples.

After observing negligible differences in crystal orientation, doping, and focusing conditions, a general discussion about the observed trends for both the amorphization and ablation thresholds as a function of laser wavelength can be initiated. Regarding the behaviors observed in Figure 7a, the analysis will be divided into two separate parts corresponding to different spectral ranges accounting for the material bandgap ($E_{g,Si}$ = 1.12 eV): from λ = 258 to 1030 nm (linear absorption regime) and from λ = 1030 to 4000 nm (nonlinear absorption regime).

First, the amorphization thresholds from UV to IR (λ = 258, 515, and 1030 nm) show an increasing trend, and it is interesting to notice one of the lowest-ever reported fluence threshold values for modification of silicon in this set of measurements ($F_{th,Am}$ = 28 mJ cm^{-2} for λ = 258 nm). The wavelength dependency is, however, not linear, showing an increase by a factor >3 from λ = 258 to 515 nm and by a factor of ≈2 from λ = 515 to 1030 nm (see exact values in Table 2). Since silicon exhibits linear absorption in this spectral range, the main differences between wavelengths rely on the absorption coefficients. By using the extinction coefficients (κ) from Adachi et al.,[15] it is determined that the optical penetration depth (OPD) is OPD>100 μm for λ = 1030 nm, while it is OPD = 1.4 μm for λ = 515 nm and only OPD = 10 nm for λ = 258 nm. Therefore, the significant differences in the measured thresholds can be seen as a consequence of these absorption considerations. Finally, it is also interesting to note that the measured threshold values in this range are consistent with the ones obtained by Izawa et al.[17,46] (at λ = 267, 400, and 800 nm), as shown in Figure 2.

A clear change of tendency is observed for wavelengths longer than λ = 1030 nm. A flat response is found for the fluence threshold for amorphization over a very large spectral range (from λ = 1030 to 3000 nm). The threshold values remain at about $F_{th,Am}$ = 200 ± 30 mJ cm^{-2} in this domain. At this stage, it is worth noting that, even if the photon energy is larger than the bandgap for λ = 1030 nm, two-photon absorption and impact ionization can already dominate depending on applied intensities, as theoretically demonstrated by van Driel.[40] Our measurements at λ = 1030, 1550, 2000, and 3000 nm fill a gap existing in the literature and so do not permit direct comparisons. However, it can be connected to the previously reported values by Werner et al.[19] and Kudryashov et al.[50] for wavelengths above λ = 2500 nm (see

Figure 2 for comparison). Additionally, our data support a further threshold increase at $\lambda = 4000$ nm.

A complete physical understanding of the threshold variations from NIR to MIR is of high complexity since the interaction regime becomes exclusively non-linear. Among the difficulties, one can mention the dynamics of nonlinear photoionization. For example, in a recent work, Derrien et al.[77] used time-dependent density functional theory (TDDFT) to demonstrate that the normally used framework of Keldysh photoionization theory[78] tends to underestimate the photoionization rates, as shown for ultrashort pulses at $\lambda = 3200$ nm (also data at $\lambda = 800$ and 1600 nm). Additionally, given the considered pulse duration ($\approx \tau = 200$ fs) and the required intensities for reaching material transformation in our work, the role of impact ionization is expected to be significant, as we demonstrated for the modifications of dielectrics.[25] Apart from non-linear absorption, other non-linear effects such as the Kerr effect should not be overlooked depending on the experimental configurations used to study the laser-material interaction process.[79] All these considerations highlight the challenge of developing a robust model to describe the diverse data presented in this work. In this context, it is interesting to refer to the threshold values obtained by Petrakakis et al.[58] with simulations accounting for pulses of $\tau = 200$ fs and wavelengths of $\lambda = 2200$, 2500, and 3300 nm (values in Table S2, Supporting Information and plotted in Figure 2). Even if the reported thresholds are lower than our measurements, the simulations tend to confirm the modest wavelength-dependence in the infrared domain and the increasing tendency for the longest tested wavelength in the mid-infrared. The authors attribute this effect to the dominance of 3-photon absorption at $\lambda = 3300$ nm in contrast to 2-photon absorption at $\lambda = 2200$ and 2500 nm. In our case, the increase from $\lambda = 2000$ nm to $\lambda = 3000$ nm, even if measurable, remains modest ($\Delta F_{\mathrm{th,Am}}$ (%) = 10%) in our work, and it is significantly less than the theoretical increase from $\lambda = 2500$ nm to $\lambda = 3300$ nm ($\Delta F_{\mathrm{th,Am}}$ (%) = 50%) reported by Petrakakis et al.[58] for pulses of similar duration ($\tau = 200$ fs). We observe a more pronounced increase ($\Delta F_{\mathrm{th,Am}}$ (%) = 70%) from $\lambda = 3000$ nm to $\lambda = 4000$ nm. This could also be discussed in regard to the change from a 3-photon to a 4-photon absorption regime.

For the ablation threshold values, a nearly linear increase is observed from UV to NIR. As shown in Figure 2, the reported values are in good agreement with the majority of the available data. In this case, the difference between $\lambda = 258$ nm and $\lambda = 515$ nm is approximately a factor of 1.4, and between $\lambda = 515$ nm and $\lambda = 1030$ nm, it is also ≈1.4. These changes are less drastic changes than those observed for amorphization. While the physical aspects behind this trend remain only partially understood for silicon, it is worth commenting on the behavior observed in another multi-wavelength study concentrating on indium phosphide (InP, $E_{\mathrm{g,InP}} = 1.42$ eV) by Borowiec et al..[80] In this work, for wavelengths above the bandgap of the material ($\lambda = 400$, 660, and 800 nm), a similar linear increase was obtained. Interestingly, the variation slope decreased when irradiating with photon energies below the material bandgap ($\lambda = 1330$ and 2050 nm). This resembles our results on silicon observed in Figure 7a for wavelengths of $\lambda = 1550$, 2000, and 3000 nm. Similar changes in the ablation threshold dependencies have also been observed for dielectrics in the NIR domain.[25,81,82] However, since dielectrics are transparent in the visible range, this does not support a coincidence with the material bandgap. Looking at longer wavelengths, the fluence threshold for dielectric ablation from NIR to MIR becomes even more relatively constant.[25] Therefore, the energy absorption mechanisms identified as causing dielectrics this quasi-wavelength-independent —namely, seed electrons created by tunnel ionization and the dominance of avalanche ionization[25] — do not directly transfer to the case of silicon studied here.

It should even be noticed that a further increase in the ablation fluence threshold is observed for irradiations at $\lambda = 4000$ nm, corresponding to a change of approximately $\Delta F_{\mathrm{th,Ab}}$ (%) = 60% to $\lambda = 3000$ nm. This could be directly associated with the larger non-linearity of absorption. A similar observation was made by Werner et al.[19] where a steeper increase is observed from $\lambda = 3250$ to 3750 nm ($\approx \Delta F_{\mathrm{th,Ab}}$ (%) = 30%) than the one observed from $\lambda = 2750$ to 3250 nm ($\approx \Delta F_{\mathrm{th,Ab}}$ (%) = 5%). Finally, it is striking to note that our data for ablation (but also for amorphization) only show a monotonic increase with increasing wavelength. Therefore, we cannot confirm that a maximum in the fluence threshold is (or will be) reached, as reported by Werner et al.[19] with a decrease from $\lambda = 3750$ to 4150 nm (approximately $\Delta F_{\mathrm{th,Ab}}$ (%) = −40%). While we do not question the values reported by other authors, the abrupt behavior observed in a modest spectral window appears somewhat surprising in comparison to our results. To comment on this issue, we discuss in Subsection 5.3 technical questions specific to the MIR range for valid measurements. Given the very few available data for comparisons in this domain, we believe it is important to account for these aspects for tentative detailed interpretations.

Finally, the ratio between modification thresholds ($F_{\mathrm{th,Ab}}/F_{\mathrm{th,Am}}$) is represented in Figure 7b. For wavelengths between $\lambda = 515$ nm and $\lambda = 4000$ nm, values between 2 and 3 are obtained. These are similar values to those reported at $\lambda = 800$ nm for different pulse durations (Figure 5c). By looking at this ratio in more detail, a minimum at $\lambda = 1030$ nm can be observed before a moderately increasing tendency up to $\lambda = 3000$ nm. The obtained data seem to be consistent with the reported findings of Werner et al.,[19] who observed a ratio of 2.2 at $\lambda = 2750$ nm and a factor of 2.6 at $\lambda = 3750$ nm. However, the most striking observation in Figure 7b is the significant difference in the UV regime, prompting the use of a logarithmic scale for the vertical axis of Figure 7b. Those reported ratio values ($F_{\mathrm{th,Ab}} / F_{\mathrm{th,Am}} = 7 \pm 2$) are consistent with another high value reported by Izawa et al.[46] at $\lambda = 267$ nm ($F_{\mathrm{th,Ab}} / F_{\mathrm{th,Am}} = 4.5$). To the best of our knowledge, the origin of this large ratio and so this large processing window for amorphization has not been investigated yet.

To try to find a possible origin for this observation, we rely on the thermodynamic limits for modification. To meet the amorphization threshold, the deposited energy must be sufficient for the surface to reach the melting temperature ($T_{\mathrm{M}} = 1687$ K). As reported by Jarutis et al.[43] using classical thermodynamic equations, the energy density needed is $\rho_{\mathrm{E,\,M}} = 3.0$ nJ µm^{-3}. The criterion for ablation is more uncertain, given that the ablation process occurs in non-equilibrium thermodynamic conditions.[83] Nonetheless, a first approximation can consist of associating the ablation limit associated with the boiling temperature ($T_{\mathrm{B}} = 3538$ K). The corresponding absorbed energy density required is then $\rho_{\mathrm{E,\,B}} = 11.3$ nJ µm^{-3}.[43] This estimate accounts for heating the solid phase up to T_{M}, then the solid-liquid phase

transition (latent heat), and finally heating the liquid up to T_B. The resulting ratio $\rho_{E,\,B}/\rho_{E,M}$ implies that ablation of silicon requires 3.8 times more deposited energy than amorphization. Taking into account non-linear absorption effects, it would not be surprising to obtain $F_{th,Ab}/F_{th,Am}$ ratios smaller or equal than $\rho_{E,\,B}/\rho_{E,M} = 3.8$, in line with the experimental data shown in Figure 7b for the wavelength range between $\lambda = 515$ and 4000 nm ($2 < F_{th,Ab}/F_{th,Am} < 3$). However, obtaining values much >3.8, as reported for UV irradiation ($F_{th,Ab}/F_{th,Am} \approx 7$) seems more anomalous.

Such a high value suggests a higher "material resistance" to ablation, which we assume is a result of an ultrashort redistribution of the deposited energy into a larger volume. It is worth considering that photon absorption at $\lambda = 258$ nm is confined in a skin-depth layer of only OPD = 10 nm. Nevertheless, this highly localized deposited energy can be redistributed into a larger volume via free-electron diffusion at ultrashort time scales. The work on electron dynamics in metals (similar to OPD as in our case) by Hohlfeld et al.[84] can be used to illustrate this aspect. It shows that two electron diffusion processes take place before electron-phonon coupling appears. First, the propagation in depth (Δz) of hot electrons reaches Δz<20 nm (speed of $<10^4$ m^{-1} s) within 200 fs (our pulse duration). Second, the propagation of ballistic electrons reaches Δz ≈2 μm (speed of ≈10^6 m^{-1} s) within 200 fs. Considering those in-depth propagation and penetration speeds (probably overestimated for silicon), we propose ultrafast electron diffusion (hot electrons or ballistics electrons) can be present in our conditions using UV ultrashort laser excitation of Si and is responsible for the energy redistribution into a larger volume that leads to an anomalously high ablation threshold.

While the above-described mechanism of hot or ballistic electron-induced increase of the heated volume appears to us as the most plausible mechanism for the very high ablation threshold at $\lambda = 258$ nm, another mechanism should be mentioned that might be present and contribute in the same direction. This mechanism would be an instantaneous strong reduction of the linear absorption coefficient at high pulse intensities. While such behavior might sound somehow exotic, it is actually exploited in so-called saturable absorbers employed to enable mode locking of ultrafast lasers.[85] These materials, typically multilayer systems, absorb strongly for low-intensity light but become, above a certain fluence threshold F_0 more transparent for high-intensity pulses. This behavior of the absorption A can be expressed as $A = 4{\cdot}\pi\ k\ /\ (\lambda{\cdot}(1 + F/F_0))$, with k being the linear optical absorption coefficient. Although we are not aware of such a "bleaching" phenomenon in Si, we cannot rule it out. In any case, more investigation is needed to clarify the underlying mechanisms, being based on ultrafast electron diffusion or saturable absorption.

3.3.2. Maximum Amorphization Depth as a Function of Laser Wavelength and Crystal Orientation

As done for the study on the influence of the pulse duration shown in Subsection 3.2.2, we have also performed an investigation of the maximum amorphization depth as a function of irradiation wavelength. This work is a continuation of the results described.[21] In that work, we determined the maximum amorphization depth from $\lambda = 515$ nm to $\lambda = 4000$ nm in Si(111) (n-type. 0.002-0.005 Ω·cm). To this end, optical microscopy images of laser-amorphized regions at fluences just below the ablation threshold were recorded upon illumination at $\lambda_{LED} = 810$ nm. The quantitative analysis yields a maximum achievable value of $d_{a\text{-}Si} = 83$ nm with single-pulse irradiation at $\lambda = 3000$ nm which can be compared to the values of $d_{a\text{-}Si} = 66$ nm obtained with irradiation at $\lambda = 1030$ nm. It is worth emphasizing that the thickness can be increased considerably further by using additional strategies, such as the use of multiple laser pulses and employing a dielectric cover layer to enhance heat extraction. Accordingly, the maximum amorphization thickness of $d_{a\text{-}Si} = 128$ nm is today demonstrated.[21]

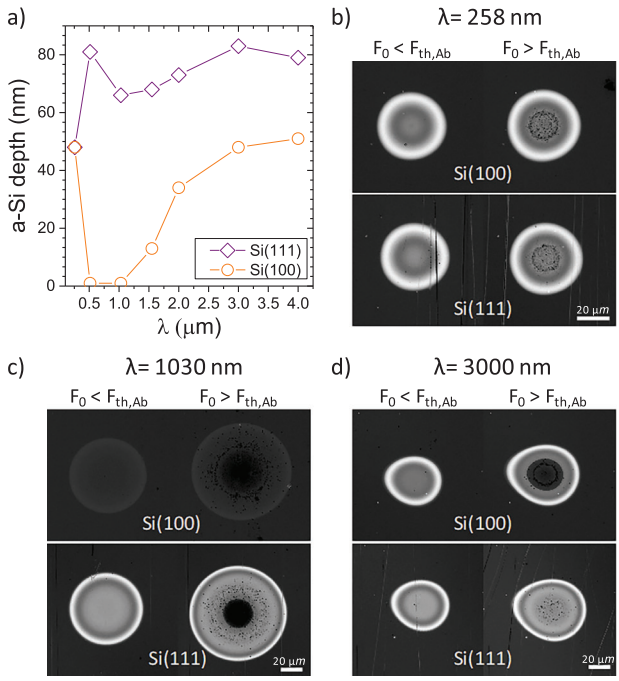

Figure 8. a) Amorphous layer thickness as a function of laser wavelength for single pulse irradiations. The thickness values are extracted from reflectivity calculations compared to microscopy images taken at the highest fluence level below the upper limit for amorphization (ablation or recrystallization). Samples: Si(111) (n-type. 0.002-0.005 Ω·cm) and Si(100) (intrinsic. 200–600 Ω·cm). b–d) Optical microscopy images of laser-induced modifications at different irradiation wavelengths in Si(111) and Si(100) (both intrinsic) were obtained with illumination at $\lambda_{LED} = 460$ nm. The spots correspond to modifications at peak fluences close (below and above) to the threshold for ablation (b) $F_0 = 200$ and 260 mJ cm^{-2}; c) $F_0 = 330$ and 480 J cm^{-2}; d) $F_0 = 490$ and 720 J cm^{-2}). The image contrast in all cases is set to display reflectivity levels in the range [0.95, 1.30].

In this work, we add the study at $\lambda = 258$ nm for Si(111), presented together with the other wavelengths in **Figure** 8a (purple). We also perform a full spectral study for Si(100) (Figure 8a, orange). The results show a noticeable influence on the crystal orientation despite the similar fluence threshold values for amorphization and ablation reported in Subsection 3.3.1. To delve deeper into this, Figure 8b–d shows a comparison of optical microscopy images of amorphous spots in Si(100) and Si(111) obtained after irradiation with single laser pulses at very different laser wavelengths.

When irradiating at fluences slightly below the ablation threshold ($F_0 < F_{th,Ab}$), a striking similarity of spots in Si(100) with spots in Si(111) can be observed for irradiation at $\lambda = 258$ nm (Figure 8b), displaying an almost identical ring structure with approximately the same brightness value in the center, indicative of the same amorphization depth. As shown in Figure 8a, the corresponding value of the amorphization depth is $d_{a\text{-}Si} = 48$ nm. Taking into account that the optical penetration depth at this wavelength is only OPD = 10 nm, this can be taken as further confirmation that the energy deposited initially in the electron system is redistributed through ultrafast electron diffusion and/or ballistic electrons, as discussed in the previous section.

At $\lambda = 3000$ nm at $F_0 < F_{th,Ab}$ (left part of Figure 8d), the ring structure is also very similar for both crystal orientations, but a brighter central disk can be observed for Si(111), indicative of a slightly thicker amorphous layer. The strongest differences in amorphization behavior for the two crystal structures at $F_0 < F_{th,Ab}$ are observed for irradiation at $\lambda = 1030$ nm (left part of Figure 8c). Here, only for Si(111) a clear signature of an amorphous surface layer can be observed. Conversely, for Si(100) the corresponding imprint has a very weak contrast (R_{rel}<1.03), which indicates either an extremely small thickness ($d_{a\text{-}Si} < 2$ nm) or an incomplete amorphization with the presence of crystalline material within the layer. When irradiating at $\lambda = 515$ nm, similar to the behavior observed at $\lambda = 1030$ nm is seen, as depicted in Figure 8a.

Figure 8b–d also presents optical microscopy images of modifications for irradiations above the ablation threshold ($F_0 > F_{th,Ab}$). The comparison with the corresponding images below the threshold ($F_0 < F_{th,Ab}$) reveals for all cases considerable surface contamination by redeposition of the ablated products. For technological considerations, this underlines the potential of laser inscription or marking via amorphization, which is inherently debris-free. Moreover, some images recorded in the ablation regime, for instance, Figure 8d for $\lambda = 3000$ nm in Si(100), display central regions with the same reflectivity as the non-irradiated crystalline area ($R_{rel} = 1$). Accordingly, it corresponds to the before-mentioned regime of recrystallization. Although this regime is not the subject of the present paper, we want to remind the reader that the recrystallization process is observed in a fluence range distinct from the one for ablation (as noted in Figure 2), an aspect that can be directly seen with these new measurements. Regarding the other wavelengths for which the images for Si(100) are not shown in Figure 8, it is interesting to mention that for $\lambda = 1550$, 2000, and 4000 nm (see **Figure 10**a for this wavelength), the fluence range for recrystallization ($F_{th,Rec}$) is below the ablation fluence threshold ($F_{th,Rec} < F_{th,Ab}$). Then, recrystallization becomes the limiting effect for the amorphization. This could potentially explain the smaller amorphous thickness observed for Si(100), as shown in Figure 8a. Again, for $\lambda = 258$ nm, an exception occurs, with $F_{th,Rec} > F_{th,Ab}$.

Besides the case of Si(100), recrystallization also occurs in Si(111) across the entire explored spectral range (see Figures 3 or 10). However, it is always in a fluence range above the fluence threshold for ablation ($F_{th,Rec} > F_{th,Ab}$). Thus, it can be concluded that recrystallization strongly depends on the laser wavelength and crystal orientation, but other parameters must also play a role (e.g., spot size). Depending on conditions, either recrystallization or ablation will define a fluence limit (the maximum that should not be exceeded) for silicon amorphization.

3.3.3. Nonlinear Absorption versus Spatial Resolution

We have discussed in the previous section the influence of the laser wavelength on the silicon amorphization depth, which corresponds to depth resolution for processing. Similarly, one expects immediately an influence of the laser wavelength on the lateral resolution. Beyond the question of the diffraction limit, one may turn intuitively to the concept of nonlinear resolution to discuss this question in detail. This concept is highly exploited in multiphoton microscopy. It describes the narrowing of the energy deposition spot in comparison to the applied laser profiles (e.g., comparing FWHM of delivered and absorbed energy profiles) caused by the nonlinear character of absorption.[86] According to the bandgap of silicon $E_{g,Si} = 1.12$ eV, this must become increasingly important in the IR domain, in which energy deposition is initiated by high-order multiphoton absorption.

The question regarding non-linear absorption and its potential benefits on lateral resolution in surface processing has recently been investigated for dielectrics by Garcia-Lechuga et al. in 2020[26] and further extended by Zhou in 2021 to semiconductors and metals.[87] Both groups demonstrated that non-linear absorption does not lead to a reduction of the ablation crater diameter. While this finding may depend on the type of material transformations, our analysis presented here investigates a possible influence of non-linear absorption on the diameter of laser-amorphized regions in silicon. In **Figure 9**, we show results obtained at $\lambda = 1550$ nm corresponding to the nonlinear absorption regime for silicon. Independent of this nonlinearity of interaction, we find a systematic one-to-one mapping between the produced features (Figure 9a), and the experimental beam profile at the sample surface (Figure 9b). By comparing the part of the beam ("beam contours") above, respectively, the amorphization and ablation thresholds ("beam sectioning" strategy illustrated in Figure 9c) we find an excellent correspondence with the induced modifications. The size and potential defects or dissymmetry affecting the beam profiles at the considered threshold values (Figure 9d) are reproduced in the material modifications (Figure 9a). Therefore, such an experiment shows that no benefit from increased nonlinearity is observed for femtosecond laser amorphization and ablation on silicon. Because these are pure threshold-based binary responses (amorphized or not, ablated or not), the local transformations only depend on the applied fluence, leading to a result independent of the absorption physics. While we show here results obtained at $\lambda = 1550$ nm, we derived similar conclusions with analyses from $\lambda = 258$ nm to 4 µm at typical $\tau = 200$ fs.

There are important consequences of these strict threshold-based and deterministic transformation responses: i) First is technological, as it becomes possible to derive the processing precision (including resolution and repeatability) by simply accounting for spot size and pulse-to-pulse energy fluctuations without any consideration of the interaction physics.[88] ii) Second, it fully justifies the local fluence analysis made in this work so that one can extract from a single Gaussian spot irradiation the depen-

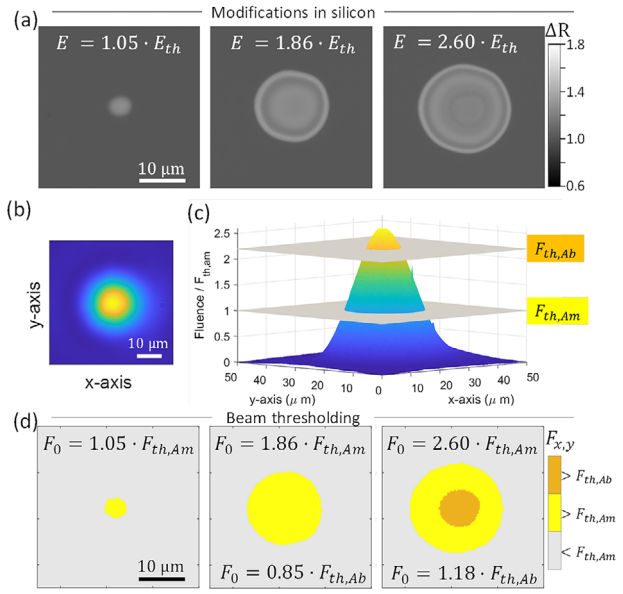

Figure 9. a) Optical microscope images of laser-induced modifications on silicon (Si(111) n-type 1–10 ohm cm with a SiO_2 layer of 1 µm) after single-pulse irradiation (λ = 1550 nm, τ = 190 fs) at different irradiation energies above the amorphization threshold. The corresponding irradiation energies are 0.89, 1.58, and 2.21 µJ. b) The 2D intensity distribution of the beam at the sample position was recorded with an InGaAs 2D sensor. c) Intensity distribution (identical to (b)) is represented along an illustration of the sectioning strategy used to extract the beam contours above the fluence threshold of amorphization and ablation. The ablation threshold is set at 2.20 times the amorphization threshold, as experimentally obtained. The peak fluence of the represented intensity profile corresponds to 2.60·$F_{th,Am}$. d) Beam contours representing the regions above $F_{th,Am}$ (yellow) and $F_{th,Ab}$ (orange) at different excitation levels (same as the modifications shown in (a)).

dence of the material response up to the peak applied fluence by space resolved analyses (see, for instance, Figure 6 on the amorphization depth).

Expanding on the technological considerations, one should keep in mind that the smallest features will always be produced by applying beams with a peak fluence just above the modification threshold. This defines a reproducibility limit imposed by the pulse-to-pulse intensity fluctuation of the laser technology used for the irradiation. This led recently to the use of stabilized fundamental beams for technological demonstrations on high-resolution laser writing by amorphization of silicon.[89]

4. Conclusion

Understanding the limits of silicon amorphization with ultrashort laser pulses is of interest for improved performance material processing solutions. It involves aspects such as the applicable range of fluences for amorphization, the conditions for maximizing the achievable thickness, and controlling the spatial resolution of the produced feature. In our study, we have thoroughly explored the subject, incorporating a new full set of data in unexplored ranges of parameters. We revealed and discussed the influence of the pulse duration (ranging from τ = 13.9 to 134 fs at λ = 800 nm) and the impact of the laser wavelength (ranging from λ = 258 to 4000 nm with τ = 200 fs). The new datasets are accompanied by detailed methodological aspects that are important for the proper identification of the different thresholds for permanent modifications (amorphization, ablation, and recrystallization) using optical microscopy and atomic force microscopy. Moreover, we have experimentally demonstrated the validity of the commonly assumed correlation between the thresholds for amorphization and melting by time-resolved microscopy measurements.

In our pulse-duration-dependent study, we found that the range of fluences leading to amorphization of Si(111) is constrained by the ablation threshold. In this context, we observed that, across all explored cases, the ablation fluence threshold is consistently about twice that of the amorphization fluence threshold. Similarly, the maximum amorphization depth remains around $d_{a\text{-}Si}$ = 80 nm for all cases, with a slight tendency toward reduced thicknesses for longer pulse durations. More differences become more notable when reporting on the fluence threshold values for amorphization. We observe a two-fold increase when comparing the measured threshold at τ = 13.9 fs ($F_{th,Am}$ = 82 mJ cm^{-2}) to the one at τ = 134 fs ($F_{th,Am}$ = 160 mJ cm^{-2}). This tendency is consistent with the expectedly increased photoionization yields as the pulses get shorter. It highlights the dominance of strong field nonlinear absorption for ultrashort pulses in this spectral range. Additionally, we believe that the presented measurements for pulses shorter than τ = 50 fs should be of interest for the validity demonstration of currently developed theoretical models.

In our wavelength-dependent study, we discussed data for Si(100) and Si(111) with various doping levels. For the fluence thresholds (amorphization and ablation), we found either no difference or very small ones (max. 12%) between samples. Regarding the influence of wavelength, we observed typically one order of magnitude difference in amorphization fluence threshold values from the UV to the MIR range. Specifically, taking advantage of the efficiency of linear absorption at λ = 258 nm, we report on the lowest ever reported threshold value for amorphization using tabletop lasers ($F_{th,Am} \approx$ 30 mJ cm^{-2}). Besides this dramatic difference when comparing the shortest and longest tested wavelengths, we have also interestingly noted a relatively flat response ($F_{th,Am} \approx$ 200 mJ cm^{-2}) over a larger part of the spectrum, covering from λ = 1030 nm to λ = 3000 nm. This range corresponds to conditions where 2-photon or 3-photon absorption processes should dominate to initiate energy deposition. Regarding the case for ablation, we have found that the threshold variations for silicon are similar to those reported for other semiconductors (e.g., InP). In brief, two linear dependencies with different slopes depending on the wavelengths correspond to photon energies above (UV to NIR) or below (NIR to MIR) the energy bandgap.

Analyses of the maximum amorphization depths depending on experimental conditions indicate that thicker amorphous layers can be obtained in Si(111). This is attributed to the upper fluence limit for amorphization, which for Si(111) is defined by ablation and for Si(100) by recrystallization. The sole exception to this picture is with the use of UV-pulses, where both materials behave very similarly. In this case, the ratio $F_{th,Ab}$ /$F_{th,Am}$ that describes the processing window becomes extremely large (≈ 7). This tends to demonstrate the importance of ultrafast electron diffusion/propagation processes in the UV regimes. These pro-

cesses enlarge the excited volume before electron-phonon coupling and thus must be responsible for this opening of an enormous fluence window for amorphization. The latter is of particular importance for technology developments as fine-tuning the amorphization depth becomes accessible by controlling the irradiation fluence.

Finally, looking not only at the modified depths but also at aspects related to lateral spatial resolution, we found no net benefit from increased interaction nonlinearities when exploring the infrared domain of the spectrum. This contrasts with results obtained in other fields, such as nonlinear microscopy, but which in laser processing cannot be applied given the strict threshold-based material transformation. This conclusion is valid for femtosecond laser amorphization and ablation under the wide range of investigated conditions.

In conclusion, the extensive sets of data gathered here on the pulse-duration and laser-wavelength dependencies of silicon responses are expected to serve as benchmarks for developing predictive models. Important efforts remain needed to improve the precision and robustness of simulation solutions. It also holds potential for advances in process engineering by fostering the integration of femtosecond laser processes in "silicon photonics" and other semiconductor technology sectors.

5. Experimental Section

Time-Resolved Microscopy Experiment: The fs-resolved microscopy experiments were done using an experimental layout essentially similar to the one reported in the references.[90–92] It was based on the initial approach by Downer and coworkers[93] and later refined and improved by Sokolowski-Tinten et al..[94]

The approach combines a pump-probe technique with wide-field microscopy in order to obtain snapshots of the temporal evolution of surface reflectivity with high spatial resolution (close to 1 µm). The experiment employs a Titanium Sapphire fs-regenerative amplifier delivering pulses of τ = 120 fs at λ = 800 nm (100 Hz repetition rate). A shutter enabled to selection of single pulses that were split into two pulses using a polarizing beam splitter. An intense IR pump pulse (λ_{pump} = 800 nm) and a weaker frequency doubled probe pulse (λ_{probe} = 400 nm) were used respectively for sample irradiation and in situ time-resolved reflection microscopy. The sketch of the experimental setup could be found elsewhere.[95]

In brief, after focusing with a 150 mm focal length, the pump pulse beam reaches the sample at an angle of incidence of θ = 52° and p-polarization. As a consequence, the apparent spot shape at the surface was Gaussian elliptical. Depending on the circular aperture used before the lens, the spot radius at $1/e^2$ was 85 µm × 50 µm (aperture diameter of 2 mm) or 52 µm × 32 µm (aperture diameter of 3.5 mm). These values were obtained by using the method described by Liu.[75] At a variable and controllable time delay, a low-intensity probe pulse at λ = 400 nm illuminates the sample surface at normal incidence after passing through a beam expander. The reflected probe pulse light forms an image onto a 12-bit CCD camera.

For each delay value between the pump and probe pulses, a set of three images was acquired blocking and unblocking the pump beam. The images were normalized to the image acquired with the pump beam blocked before irradiating the surface. This enables to register of two normalized images corresponding to the relative changes of reflectivity of the illuminated surface at the established delay value and a few seconds after irradiation. From the pump beam profile, the local fluence experienced by different regions of the excited surface could be easily computed, while the normalized reflectivity images can be transformed to real reflectivity values corresponding to the non-excited surface, as thoroughly described.[96]

Pulse-Duration Tunable Laser System and Irradiation Conditions: The beamline 5a of ASUR platform (λ = 800 nm, $\Delta\lambda \cong$ 760–840 nm, $\tau \cong$ 25-fs FWHM nominal pulse duration, linear polarization)[97] delivering maximum energy of 1 mJ with 1% root mean square (rms) fluctuations was used to study the metrics of laser-induced modification thresholds of silicon in the single-shot regime and at normal incidence. Laser conditions of the experiment (pulse duration and spot size on target) were characterized using second-order autocorrelation and beam imaging measurements to ensure a reliable parametric study of silicon modifications in the ultrashort regime. To get longer pulse durations, the nominal beam was pre-chirped through compressor grating adjustments, providing for this study pulse duration parameters from $\tau \approx$25 to $\tau \approx$135 fs, as measured by a single-shot Bonsai (Amplitude Laser) second-order autocorrelator system. To access the shortest pulse duration (τ = 13.9 fs), the cross-polarized wave XPW technique[98] was implemented using two BaF_2 crystals placed in a vacuum tube to broaden the beam spectrum ($\Delta\lambda$ = 720 – 880 nm) at the same operating central wavelength (λ = 800 nm). The spectrally enlarged XPW signal was then filtered from the pump by a succession of thin Brewster fused silica polarizer plates. The pulse compression to the ultrashort pulse duration, τ = 13.9 fs, was further achieved using an ensemble of chirped mirrors and a pair of fused silica wedges. The delivery of pulses of τ = 13.9 fs to the target was controlled by a Femtometer (Femtolasers Gmbh) second-order autocorrelator positioned just before the focusing parabolic mirror and thus considering all the dispersive optics used before reaching the sample. The energy fluctuations for the pulses of τ = 13.9 fs pulses were slightly higher than those of the nominal pump pulses, being ≅ 1.6% rms

To perform the study, the characteristics of laser amorphization and damage of silicon under a wide set of laser conditions, with pulse duration varied from τ = 13.9 to 134 fs were explored. To ensure the reliable evaluation of the corresponding material thresholds under this large temporal range, the same setup and diagnostics were used for each tested condition. Details of this test-bench operated in the air can be found.[99] Another important piece of information for the reader was about beam focusing. It was done at normal incidence using an off-axis parabolic mirror of 152.4 mm effective focal length, and the incident energy was taken as the driving parameter to induce the changes in the samples. Statistics on five independent tests were performed for each irradiation condition in order to provide solid results.

Wavelength Tunable Laser System and Irradiation Conditions: The methodology used to study the wavelength dependence of silicon modifications was very similar to the one described.[25] for a previous work concentrating on the ablation of dielectrics. In this previous paper, a sketch summarizes the experimental configuration employed to deliver femtosecond laser beams at various wavelengths from λ = 258 nm to 4.5 µm while tentatively maintaining similar other characteristics (in particular the pulse duration) for reliable relative comparisons.

The setup uses as a master laser a commercial femtosecond amplifier (Pharos, Light Conversion) emitting at λ = 1030 nm pulses with energies up to 500 µJ. The pulse duration was τ = 180 ± 10 fs at full-width at half maximum (FWHM), as characterized by single-shot autocorrelation (TiPA, Light conversion). Visible (VIS) and ultraviolet (UV) radiations (λ = 515 and 258 nm) were simply obtained through second and fourth harmonic generation (Hiro, Light Conversion). The pulse duration at λ = 515 nm was measured at τ = 160 ± 10 fs FWHM. A similar pulse duration was also expected at λ = 258 nm according to the design (thickness) of the last doubling crystal. For infrared radiations, an optical parametric amplifier (OPA, Orpheus, Light Conversion) was relied upon, designed for efficient conversion over a large infrared range (signal: λ = 1.5 to 2.06 µm, idler: λ = 2.06 to 4.5 µm). Using the already mentioned autocorrelator device, pulse durations of τ = 190 ± 10 fs FWHM were measured in the range covered by the signal beams. A direct correspondence of the pulse duration was expected for the idler beams according to the parametric amplification process.

For each selected wavelength, the beam was directed toward the same irradiation beam line. Gold mirrors were used for the OPA beams. The other beams were systematically replaced by specific high-reflectivity dielectric mirrors to reduce energy losses and ensure excellent spectral fil-

tering at the considered wavelength. For all the wavelengths, the beam irradiates the target at normal incidence with linear polarization. Depending on the beams, different focusing conditions were used as described in Table S3 (Supporting Information). The choices for the lens materials and focal distances were made to ensure sufficient fluences on relatively large spots (w_0>10 μm) so that the same ex situ characterization methodology can be used for all the analyses. For well-defined spot profiles impinging on silicon surface, an iris diaphragm was placed before the lens to truncate all beams (transmitted power < 75%). This was of particular importance to suppress potential biases caused by some of the OPA beam profiles exhibiting pedestals.[76]

The sample was mounted on an XYZ motorized stage and aligned perpendicular to the irradiation axis. Motion in the XY plane, perpendicular to the axis of laser incidence, allows to position of the sample on a fresh surface before each irradiation. The optimal focusing position was determined by a Z-scanning procedure and real-time surface imaging with a tilted microscopy arrangement (10× microscope objective, tube lens, and CCD-camera, angle of 45° with respect to laser optical axis). The ≈10-μm depth-of-field of the same in situ microscopy system was also used for precise sample repositioning between irradiation experiments.

The single-shot operation was controlled using a pulse-picker integrated into the master laser. To control the pulse energy in the broadband domain of this work, a set of neutral-density metallic filters (1 mm UV-fused silica substrate with silver coating) mounted on a motorized wheel was relied upon. Calibration measurements of filter transmissions were made for all applied beams at a 1 kHz repetition rate using a thermal powermeter (3A, Ophir). Peak-to-peak pulse energy stability was evaluated using a pyroelectric energy meter (PE9-C, Ophir) to be <4% for all the considered wavelengths. The reported fluence values account for the Fresnel reflection losses expected on the lens surfaces.

It should be noted that both the thermal power meter and pyroelectric energy meter reported equal energy measurements for pulses from λ = 258 to 2000 nm. However, a different behavior was observed at λ = 3000 nm and λ = 4000 nm, with measurements from the pyroelectric energy meter being underestimated compared to those from the thermal power meter (up to a 75% difference at λ = 4000 nm). Even when tested with different thermal power meters. While both devices (PE9 and 3A) were specified by the manufacturer to work over a large spectral range, the values measured by the thermal power meter should be more accurate, given the expected wavelength independence of the underlying physical principles for operation (absorber structure with a black coating resulting in temperature rise).

Fluence Threshold Determination Methodology: The amorphization fluence threshold ($F_{th,Am}$) was determined by the so-called D^2-method or Liu's method.[75] In this case, the modified area of each of the laser-induced modifications was represented (see examples in Figure 10a) versus the corresponding pulse energy of irradiation (in logarithmic scale). The modified area was obtained by image analysis, selecting the region contouring the increase in reflectivity due to the formation of the amorphous phase. The D^2-method or Liu's method representation, as shown in Figure 10b, leads to a linear tendency when the beam profile was Gaussian or close to it (Airy-disc-like beam shape[76]). The linear regression from these data allows to obtain the amorphization energy threshold ($E_{th,Am}$) and the radius (or waist) of a Gaussian profile at $1/e^2$ of the peak intensity (w_0). The amorphization fluence threshold was then obtained as $F_{th,Am} = 2\,E_{th,Am}/(\pi\, w_0^2)$. We remember that, to avoid imperfections on beam profiles (as pedestals observed on wavelengths generated at the OPA[26]), a circular aperture was used before the focusing lens. This results in the formation of an Airy-disc-like beam at the sample position. For accounting for this deviation from a Gaussian beam profile, the same procedure is explained.[76] had been applied.

Regarding the estimated error for fluence threshold determination in the multi-wavelength study, as indicated,[76] Liu's methodology for Airy-like beams should cause an error of not <5%. In this work, in order to be more conservative, the presented values were systematically accompanied by 10% error bars.

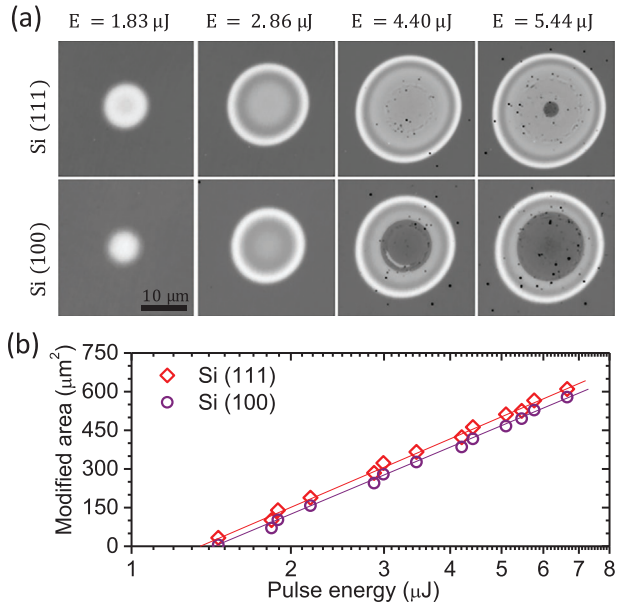

Figure 10. a) Optical microscope images of single pulse laser-induced modifications at λ = 4000 nm (τ = 200 fs) in Si(111) (n-type. 0.002-0.005 Ω·cm) and Si(100) (Intrinsic. 200–600 Ω·cm) recorded at λ_{LED} = 460 nm. The energy of the irradiation is labeled above the images. b) Liu's method or D^2-method representation for obtaining the beam waist (related to the slope) and the amorphization energy threshold. The values plotted on the *y*-axis are extracted from analyses of the images shown in (a) and some others at different pulse energies.

The determination of the ablation fluence threshold ($F_{th,Ab}$) was performed through the characterization of the ablated region dimensions (see diameters of ablation, ϕ_{Ab}, in Figure 2). The ablation fluence threshold was then obtained by a local fluence analysis following the expression: $F_{th,Ab} = F_0\ exp(-\frac{2\,(\phi_{Ab}/2)^2}{w_0^2})$, where ϕ_{Ab} corresponds to the diameter of the ablated region at a given peak fluence, F_0. The peak fluence was obtained as $F_0 = 2E/(\pi\, w_0^2)$, being E the pulse energy and w_0 the beam characteristics extracted from Liu's method applied on the amorphous region (Figure 10b).

Amorphous Layer Thickness Determination Metrology: The laser-irradiated samples were characterized using an optical microscope in reflection, employing monochromatic illumination sources at various wavelengths. This method was frequently used for assessing the thickness of the amorphous layer, $d_{a\text{-}Si}$, formed in silicon,[16,18,21] since its presence leads to the appearance of interference fringes in the microscope image. These fringes result from the interference between light reflected at the sample surface and light reflected at the embedded amorphous/crystalline interface. The microscope used was a Nikon Eclipse Ti equipped with a 100×, 0.9 N.A. objective lens, and a 12-bit CCD camera, employing switchable LED illumination at λ_{LED} = 460 and 810 nm wavelengths.

The modeling to ascertain the thickness of the amorphous layer was conducted using Fresnel equations. The developed program relies on a precise mathematical description of the interaction between an electromagnetic wave and an isotropic planar multilayered system, commonly known as Abeles' theory.[100] Each layer was computed to have a given thickness and optical properties (refractive index and absorption coefficients). The optical constants at the wavelengths used by the LED illumination were taken from[15] and were previously listed.[21] The calculation of the reflectivity of the whole system at the illumination wavelength of λ_{LED} = 810 nm as a function of the amorphous layer thickness was shown in the inset of Figure 5c. It was computationally obtained after transforming layer by layer in steps of 1 nm the optical constants of c-Si into those of a-Si.

Supporting Information

Supporting Information is available from the Wiley Online Library or from the author.

Acknowledgements

This work was conducted using ASUR and LaMP facilities at LP3. It has been supported by the European Union's H2020 program (Grant agreements Laserlab-Europe No 871124 [project CNRS-LP3002792 and CNRS-LP300258] and ERC No 871124), grant HyperSolar (TED2021–130894B-C22) funded by MCIN/AEI/10.13039/501100011033 by "European Union NextGenerationEU/PRTR", grant ULS_PSB (PID2020-112770RB-C21) funded by MCIN/AEI/10.13039/501100011033, .and grant ANR-23-CE08-0029-03 funded by French National Research Agency (ANR). It was also partially funded by the CSIC through the call for internationalization i-LINK 2022 (project ILINK22056). N. Casquero acknowledges a pre-doctoral fellowship from the MICINN. The authors acknowledge F. Chacón (Instituto de Óptica, CSIC) for AFM measurement.

Conflict of Interest

The authors declare no conflict of interest.

Data Availability Statement

The data that support the findings of this study are available from the corresponding author upon reasonable request.

Keywords

femtosecond laser-matter interactions, few-optical-cycle pulses, silicon amorphization, Silicon photonics, wavelength tunable lasers

Received: December 15, 2023
Revised: June 11, 2024
Published online:

[1] *Handbook of Semiconductor Manufacturing Technology*, (Eds.: R. Doering, Y. Nishi), CRC Press, USA **2017**.
[2] J. M. Warrender, *Appl. Phys. Rev.* **2016**, *3*, 031104.
[3] F. Priolo, T. Gregorkiewicz, M. Galli, T. F. Krauss, *Nat. Nanotechnol.* **2014**, *9*, 19.
[4] M. Notomi, *Reports Prog. Phys.* **2010**, *73*, 096501.
[5] R. Halir, P. J. Bock, P. Cheben, A. Ortega-Moñux, C. Alonso-Ramos, J. H. Schmid, J. Lapointe, D. Xu, J. G. Wangüemert-Pérez, Í. Molina-Fernández, S. Janz, *Laser Photon. Rev.* **2015**, *9*, 25.
[6] M. Chambonneau, D. Grojo, O. Tokel, F. Ö Ilday, S. Tzortzakis, S. Nolte, *Laser Photon. Rev.* **2021**, *15*, 2100140.
[7] D. Grojo, M. Chambonneau, S. Lei, A. Mouskeftaras, O. Utéza, A. Wang, in *Ultrafast Laser Nanostructuring Purs. Extrem. Scales*, (Eds.: R. Stoian, J. Bonse), Springer International Publishing, Cham, **2023**, 979.
[8] M. O. Thompson, G. J. Galvin, J. W. Mayer, P. S. Peercy, J. M. Poate, D. C. Jacobson, A. G. Cullis, N. G. Chew, *Phys. Rev. Lett.* **1984**, *52*, 2360.
[9] P. L. Liu, R. Yen, N. Bloembergen, R. T. Hodgson, *Appl. Phys. Lett.* **1979**, *34*, 864.
[10] C. V. Shank, R. Yen, C. Hirlimann, *Phys. Rev. Lett.* **1983**, *51*, 900.
[11] A. Kiani, K. Venkatakrishnan, B. Tan, *Opt. Express* **2009**, *17*, 16518.
[12] Y. Fuentes-Edfuf, M. Garcia-Lechuga, D. Puerto, C. Florian, A. Garcia-Leis, S. Sanchez-Cortes, J. Solis, J. Siegel, *Appl. Phys. Lett.* **2017**, *110*, 211602.
[13] D. Puerto, M. Garcia-Lechuga, J. Hernandez-Rueda, A. Garcia-Leis, S. Sanchez-Cortes, J. Solis, J. Siegel, *Nanotechnology* **2016**, *27*, 265602.
[14] J. Huang, L. Jiang, X. Li, A. Wang, Z. Wang, Q. Wang, J. Hu, L. Qu, T. Cui, Y. Lu, *Nanophotonics* **2019**, *8*, 869.
[15] S. Adachi, *Optical Constants of Crystalline and Amorphous Semiconductors*, Springer US, Boston, MA, **1999**.
[16] J. Bonse, *Appl Phys A Mater Sci Process* **2006**, *84*, 63.
[17] Y. Izawa, Y. Izawa, Y. Setsuhara, M. Hashida, M. Fujita, R. Sasaki, H. Nagai, M. Yoshida, *Appl. Phys. Lett.* **2007**, *90*, 2006.
[18] Y. Fuentes-Edfuf, M. Garcia-Lechuga, D. Puerto, C. Florian, A. Garcia-Leis, S. Sanchez-Cortes, J. Solis, J. Siegel, *Sci. Rep.* **2017**, *7*, 4594.
[19] K. Werner, V. Gruzdev, N. Talisa, K. Kafka, D. Austin, C. M. Liebig, E. Chowdhury, *Sci. Rep.* **2019**, *9*, 19993.
[20] C. Florian, D. Fischer, K. Freiberg, M. Duwe, M. Sahre, S. Schneider, A. Hertwig, J. Krüger, M. Rettenmayr, U. Beck, A. Undisz, J. Bonse, *Materials* **2021**, *14*, 1651.
[21] M. Garcia-Lechuga, N. Casquero, A. Wang, D. Grojo, J. Siegel, *Adv. Opt. Mater.* **2021**, *9*, 2100400.
[22] J. Bonse, K. W. Brzezinka, A. J. Meixner, *Appl. Surf. Sci.* **2004**, *221*, 215.
[23] M. O. Thompson, J. W. Mayer, A. G. Cullis, H. C. Webber, N. G. Chew, J. M. Poate, D. C. Jacobson, *Phys. Rev. Lett.* **1983**, *50*, 896.
[24] J. A. Yater, M. O. Thompson, *Phys. Rev. Lett.* **1989**, *63*, 2088.
[25] M. Garcia-Lechuga, O. Utéza, N. Sanner, D. Grojo, *Phys. Rev. Appl.* **2023**, *19*, 044047.
[26] M. Garcia-Lechuga, O. Utéza, N. Sanner, D. Grojo, *Opt. Lett.* **2020**, *45*, 952.
[27] P. P. Pronko, P. A. VanRompay, C. Horvath, F. Loesel, T. Juhasz, X. Liu, G. Mourou, *Phys. Rev. B* **1998**, *58*, 2387.
[28] J. Bonse, S. Baudach, J. Krüger, W. Kautek, M. Lenzner, *Appl Phys A Mater Sci Process* **2002**, *74*, 19.
[29] H. O. Jeschke, M. E. Garcia, M. Lenzner, J. Bonse, J. Krüger, W. Kautek, *Appl. Surf. Sci.* **2002**, *197–198*, 839.
[30] A. Borowiec, M. Mackenzie, G. C. Weatherly, H. K. Haugen, *Appl Phys A Mater Sci Process* **2003**, *76*, 201.
[31] P. Allenspacher, B. Huettner, W. Riede, *Laser-Induced Damage Opt. Mater. 2002 7th Int. Work. Laser Beam Opt. Charact.* **2003**, *4932*, 358.
[32] S. Besner, J. Y. Degorce, A. V. Kabashin, M. Meunier, *Appl. Surf. Sci.* **2005**, *247*, 163.
[33] T. Rublack, G. Seifert, *Opt. Mater. Express* **2011**, *1*, 543.
[34] S. Leyder, *Ionisation Nonlinéaire Dans Les Matériaux Diélectriques et Semiconducteurs Par Laser Femtoseconde Accordable Dans Le Proche Infrarouge*, Aix-Marseille Université, France **2013**.
[35] X. L. Liu, W. Cheng, M. Petrarca, P. Polynkin, *Appl. Phys. Lett.* **2016**, *109*, 161604.
[36] R. N. Oosterbeek, C. Corazza, S. Ashforth, M. C. Simpson, *Appl. Phys. A* **2016**, *122*, 449.
[37] C. S. R. Nathala, A. Ajami, W. Husinsky, B. Farooq, S. I. Kudryashov, A. Daskalova, I. Bliznakova, A. Assion, *Appl. Phys. A* **2016**, *122*, 107.
[38] R. S. Cahyadi, B. Torralva, S. M. Yalisove, *Appl. Phys. Lett.* **2018**, *112*, 032105.
[39] A. Rämer, O. Osmani, B. Rethfeld, *J. Appl. Phys.* **2014**, *116*, 053508.
[40] H. M. Van Driel, *Phys. Rev. B* **1987**, *35*, 8166.
[41] D. P. Korfiatis, K. A. T. Thoma, J. C. Vardaxoglou, *J Phys D Appl Phys* **2007**, *40*, 6803.

[42] T. Takahashi, S. Tani, R. Kuroda, Y. Kobayashi, *Appl. Phys. A* **2020**, *126*, 582.
[43] V. Jarutis, D. Paipulas, V. Jukna, *Materials (Basel)* **2023**, *16*, 2205.
[44] H. Liu, G. Mourou, T. Juhasz, in *Conf. Lasers Electro-Optics*, Optica Publishing Group, San Francisco, CA, USA **2004**.
[45] B. M. Cowan, *Proc. SPIE 6720, Laser-Induced Damage in Optical Materials: 2007*, Boulder, Colorado, United States, December **2007**.
[46] Y. Izawa, S. Tokita, M. Fujita, M. Nakai, T. Norimatsu, Y. Izawa, *J. Appl. Phys.* **2009**, *105*, 064909.
[47] D. Austin, K. Kafka, C. I. Blaga, L. F. Dimauro, E. Chowdhury, *Proc. SPIE 9237, Laser-Induced Damage in Optical Materials: 2014*, October **2014**.
[48] L. Gallais, D.-B. Douti, M. Commandré, G. Batavičiūtė, E. Pupka, M. Ščiuka, L. Smalakys, V. Sirutkaitis, A. Melninkaitis, *J. Appl. Phys.* **2015**, *117*, 223103.
[49] R. N. Oosterbeek, S. Ashforth, O. Bodley, M. C. Simpson, *Int. J. Nanotechnol.* **2017**, *14*, 313.
[50] S. I. Kudryashov, T. Pflug, N. I. Busleev, M. Olbrich, A. Horn, M. S. Kovalev, N. G. Stsepuro, *Opt. Mater. Express* **2021**, *11*, 1.
[51] J. Thorstensen, S. Erik Foss, *J. Appl. Phys.* **2012**, *112*, 103514.
[52] A. Sikora, D. Grojo, M. Sentis, *J. Appl. Phys.* **2017**, *122*, 045702.
[53] R. Agustsson, E. Arab, A. Murokh, B. O'Shea, A. Ovodenko, I. Pogorelsky, J. Rosenzweig, V. Solovyov, R. Tilton, *Opt. Mater. Express* **2015**, *5*, 2835.
[54] A. V. Bulgakov, J. Sládek, J. Hrabovský, I. Mirza, W. Marine, N. M. Bulgakova, *Appl. Surf. Sci.* **2024**, *643*, 158626.
[55] H. Vaghasiya, S. Krause, P.-T. Miclea, *J Phys D Appl Phys* **2022**, *55*, 175109.
[56] A. Cavalleri, K. Sokolowski-Tinten, J. Bialkowski, M. Schreiner, D. Von Der Linde, *J. Appl. Phys.* **1999**, *85*, 3301.
[57] R. Moser, M. Domke, J. Winter, H. P. Huber, G. Marowsky, *Adv. Opt. Technol.* **2018**, *7*, 255.
[58] E. Petrakakis, G. D. Tsibidis, E. Stratakis, *Phys. Rev. B* **2019**, *99*, 195201.
[59] N. Medvedev, B. Rethfeld, *J. Appl. Phys.* **2010**, *108*, 103112.
[60] S. Maragkaki, G. D. Tsibidis, L. Haizer, Z. Pápa, R. Flender, B. Kiss, Z. Márton, E. Stratakis, *Appl. Surf. Sci.* **2023**, *612*, 155879.
[61] N. Stojanovic, D. Von Der Linde, K. Sokolowski-Tinten, U. Zastrau, F. Perner, E. Förster, R. Sobierajski, R. Nietubyc, M. Jurek, D. Klinger, J. Pelka, J. Krzywinski, L. Juha, J. Cihelka, A. Velyhan, S. Koptyaev, V. Hajkova, J. Chalupsky, J. Kuba, T. Tschentscher, S. Toleikis, S. Düsterer, H. Redlin, *Appl. Phys. Lett.* **2006**, *89*, 30.
[62] T. Dinh, N. Medvedev, M. Ishino, T. Kitamura, N. Hasegawa, T. Otobe, T. Higashiguchi, K. Sakaue, M. Washio, T. Hatano, A. Kon, Y. Kubota, Y. Inubushi, S. Owada, T. Shibuya, B. Ziaja, M. Nishikino, *Commun. Phys.* **2019**, *2*, 150.
[63] M. von Allmen, A. Blatter, in *Laser-Beam Interactions with Materials*, Springer Berlin Heidelberg, Berlin, Heidelberg, **1995**.
[64] N. Casquero, C. Ruiz De Galarreta, Y. Fuentes-Edfuf, J. Solis, C. D. Wright, J. Siegel, *J Phys D Appl Phys* **2022**, *55*,365104.
[65] M. Garcia-Lechuga, J. Solis, J. Siegel, in *Ultrafast Laser Nanostructuring*, (Eds.: R. Stoian, J. Bonse), Springer, Cham, **2023**, 277.
[66] A. M. T. Kim, J. P. Callan, C. A. D. Roeser, E. Mazur, *Phys. Rev. B* **2002**, *66*, 245203.
[67] K. Sokolowski-Tinten, J. Bialkowski, D. von der Linde, *Phys. Rev. B* **1995**, *51*, 14186.
[68] O. P. Uteza, E. G. Gamaly, A. V. Rode, M. Samoc, B. Luther-Davies, *Phys Rev B Condens Matter Mater Phys* **2004**, *70*, 054108.
[69] P. Stampfli, K. H. Bennemann, *Phys. Rev. B* **1994**, *49*, 7299.
[70] M. Garcia-Lechuga, D. Puerto, Y. Fuentes-Edfuf, J. Solis, J. Siegel, *ACS Photonics* **2016**, *3*, 1961.
[71] M. Lenzner, J. Krüger, S. Sartania, Z. Cheng, C. Spielmann, G. Mourou, W. Kautek, F. Krausz, *Phys. Rev. Lett.* **1998**, *80*, 4076.
[72] A. C. Tien, S. Backus, H. Kapteyn, M. Murnane, G. Mourou, *Phys. Rev. Lett.* **1999**, *82*, 3883.
[73] E. G. Gamaly, A. V. Rode, B. Luther-Davies, V. T. Tikhonchuk, *Phys. Plasmas* **2002**, *9*, 949.
[74] B. Chimier, O. Utéza, N. Sanner, M. Sentis, T. Itina, P. Lassonde, F. Légaré, F. Vidal, J. C. Kieffer, *Phys. Rev. B* **2011**, *84*, 094104.
[75] J. M. Liu, *Opt. Lett.* **1982**, *7*, 196.
[76] M. Garcia-Lechuga, D. Grojo, *Open Res Eur* **2021**, *1*, 7.
[77] T. J. Y. Derrien, N. Tancogne-Dejean, V. P. Zhukov, H. Appel, A. Rubio, N. M. Bulgakova, *Phys. Rev. B* **2021**, *104*, L241201.
[78] L. V. Keldysh, *Sov. Phys. JETP* **1965**, *21*, 1135.
[79] A. D. Bristow, N. Rotenberg, H. M. Van Driel, *Appl. Phys. Lett.* **2007**, *90*, 16.
[80] A. Borowiec, H. F. Tiedje, H. K. Haugen, *Appl. Surf. Sci.* **2005**, *243*, 129.
[81] T. Q. Jia, H. X. Chen, M. Huang, F. L. Zhao, X. X. Li, S. Z. Xu, H. Y. Sun, D. H. Feng, C. B. Li, X. F. Wang, R. X. Li, Z. Z. Xu, X. K. He, H. Kuroda, *Phys. Rev. B* **2006**, *73*, 054105.
[82] G. Olivié, D. Giguère, F. Vidal, T. Ozaki, J.-C. Kieffer, O. Nada, I. Brunette, *Opt. Express* **2008**, *16*, 4121.
[83] D. von der Linde, K. Sokolowski-Tinten, *Appl. Surf. Sci.* **2000**, *154–155*, 1.
[84] J. Hohlfeld, S.-S. Wellershoff, J. Güdde, U. Conrad, V. Jähnke, E. Matthias, *Chem. Phys.* **2000**, *251*, 237.
[85] U. Keller, K. J. Weingarten, F. X. Kartner, D. Kopf, B. Braun, I. D. Jung, R. Fluck, C. Honninger, N. Matuschek, J. Aus der Au, *IEEE J. Sel. Top. Quantum Electron.* **1996**, *2*, 435.
[86] K. Sugioka, Y. Cheng, *Appl. Phys. Rev.* **2014**, *1*, 041303.
[87] B. Zhou, A. Kar, M. J. Soileau, X. Yu, *Opt. Express* **2021**, *29*, 5635.
[88] M. Garcia-Lechuga, G. Gebrayel El Reaidy, H. Ning, P. Delaporte, D. Grojo, *Appl. Phys. Lett.* **2020**, *117*, 171604.
[89] P. Sopeña, M. Garcia-Lechuga, A. Wang, D. Grojo, *Opt. Lett.* **2022**, *47*, 993.
[90] J. Bonse, G. Bachelier, J. Siegel, J. Solis, *Phys. Rev. B* **2006**, *74*, 134106.
[91] D. Puerto, W. Gawelda, J. Siegel, J. Bonse, G. Bachelier, J. Solis, *Appl. Phys. A* **2008**, *92*, 803.
[92] Y. Fuentes-Edfuf, M. Garcia-Lechuga, J. Solis, J. Siegel, *Laser Photon. Rev.* **2022**, *16*, 2200511.
[93] M. C. Downer, R. L. Fork, C. V. Shank, *J. Opt. Soc. Am. B* **1985**, *2*, 595.
[94] K. Sokolowski-Tinten, J. Bialkowski, A. Cavalleri, D. von der Linde, A. Oparin, J. Meyer-ter-Vehn, S. I. Anisimov, *Phys. Rev. Lett.* **1998**, *81*, 224.
[95] M. Garcia-Lechuga, J. Siegel, J. Hernandez-Rueda, J. Solis, *J. Appl. Phys.* **2014**, *116*, 113502.
[96] J. Siegel, J. Solis, in *Femtosecond Laser Micromach. Photonic Microfluid. Devices Transparent Mater* (Eds.: R. Osellame, G. Cerullo, R. Ramponi), Springer Berlin Heidelberg, Berlin, Heidelberg, **2012**, 19.
[97] O. Utéza, P. Blandin, L. Charmasson, G. Coustillier, D. Grojo, A. Kabashin, M. Lebugle, N. Sanner, V. Tcheremiskine, M. Sentis, F. Légaré, J. C. Kieffer, in *UVX 2012-11e Colloq. Sur Les Sources Cohérentes Incohérentes UV, VUV X; Appl. Développements Récents*, (Eds.: E. Constant, P. Martin, H. Bachau), EDP Sciences, Les Ulis, France, **2013**, 01004.
[98] A. Jullien, O. Albert, F. Burgy, G. Hamoniaux, J.-P. Rousseau, J.-P. Chambaret, F. Augé-Rochereau, G. Chériaux, J. Etchepare, N. Minkovski, S. M. Saltiel, *Opt. Lett.* **2005**, *30*, 920.
[99] T. Genieys, M. Sentis, O. Utéza, *Adv. Opt. Technol.* **2020**, *9*, 131.
[100] M. Born, E. Wolf, A. B. Bhatia, P. C. Clemmow, D. Gabor, A. R. Stokes, A. M. Taylor, P. A. Wayman, W. L. Wilcock, *Principles of Optics*, Cambridge University Press, UK **1999**.